Alma Mater Studiorum · University of Bologna

School of Science
Department of Physics and Astronomy
Master Degree in Physics

Evaluation of the systematic uncertainty related to the fit model in the ΔA_{CP} measurement at LHCb

Supervisor:
Prof. Angelo Carbone

Co-supervisor:
Dr. Marianna Fontana

Submitted by:
Gianluca Povero

Academic Year 2023/2024

Abstract

This study presents a measurement of the systematic uncertainty associated to the fit model used in the measurement of ΔA_{CP}. The measurement uses data at centre-of-mass energy of $\sqrt{s} = 13.6$ Tev collected by the upgraded LHCb experiment, during the Run 3 of LHC. By the development of an alternative model compared to the baseline model, the result obtained is:

$$\sigma_{\mathrm{syst}} = 8 \times 10^{-5}.$$

Contents

Introduction

From the start, the objective of the LHCb experiment has always been that of discovering hints of new physics, indications of what could be beyond the limits of the Standard Model (SM) which is only an effective theory. It exploits an indirect method, where possible new heavy particles could contribute to the amplitudes, thus modifying the properties of the SM observables. One such observable is the difference of CP asymmetries between $D^0 \to K^+K^-$ and $D^0 \to \pi^+\pi^-$. This observable is particularly powerful, because it is proven to be robust against possible systematic uncertainties. In this thesis the study of these decays is presented for the first time, using the data from the Run 3 of LHC. First the fit model to extract the number of signal events is presented, discussing also an alternative model in comparison to the baseline. Secondly, a systematic uncertainty is determined. The thesis is organized as follows. A solid view of the theory behind CP violation is given in Chapter 1. Chapter 2 gives a description of the upgraded LHCb detector, with a particular emphasis on the subdectors which are important for this analysis. In chapter 3 the data analysis is discussed in details, from the data selection to the fit models comparison. The systematic uncertainties assigned to the fit model is reported in the Chapter 3.4.

Chapter 1

Theory of CP violation

The Standard Model (SM) of particle physics is made by the combination of contributions which describes different sectors of nature interactions. The first one is the Glashow-Weinberg-Salam (GWS) model, a Yang-Mills non-abelian quantum field theory based on the two gauge symmetry groups SU(2) × U(1). It provides the picture of electroweak interactions and it has been experimentally proven to be a solid and successful model. The GSW model is then expanded by introducing the SU(3) gauge symmetry group which describes the strong interactions. Lastly, adding the Brout-Englert-Higgs spontaneous symmetry breaking mechanism which explain how a particle acquire mass, one obtains the SM which can describe all known particles and fundamental interactions except for gravity.

In this chapter the GSW model is described in Sec. 1.1 while Sec. 1.2 will focus on the CKM matrix. Lastly, in Sec. 1.3 the phenomenology of CP violation in neutral mesons is described, focusing on charged two-body decays of neutral D meson.

1.1 The GSW model

Looking at he Glashow-Weinberg-Salam model Lagrangian one can see that it is composed by 4 main components [1, 2, 3]

$$\mathcal{L} = \mathcal{L}_B + \mathcal{L}_f + \mathcal{L}_H + \mathcal{L}_Y. \tag{1.1}$$

The first term represents the kinetic term of the four gauge fields: W^a_μ (the weak isospin fields with $a = 1, 2, 3$) and B_μ the hypercharge field. Using field tensor notation, one can write this Lagrangian term as

$$\mathcal{L}_B = -\frac{1}{4} W^{a\mu\nu} W^a_{\mu\nu} - \frac{1}{4} B^{\mu\nu} B_{\mu\nu}, \tag{1.2}$$

where W and B are defined as the field strength tensors. These are not the physical gauge fields, one has to account for charged- and neutral-current interactions which leads to the definitions

$$W_\mu^\pm = \frac{W_\mu^1 \mp iW_\mu^2}{\sqrt{2}}, \tag{1.3a}$$

$$Z_\mu = W_\mu^3 \cos\theta_W - B_\mu \sin\theta_W, \tag{1.3b}$$

$$A_\mu = W_\mu^3 \sin\theta_W + B_\mu \cos\theta_W, \tag{1.3c}$$

where θ_W is the Weinberg angle ($\sin\theta_W \simeq 0.23$).

The second term describes the kinematics of the fermion and how they interact with the gauge bosons and is the first SM term which has an asymmetry. Using tensor notation

$$\mathcal{L}_f = \bar{Q}^j i\not{D}_L Q^j + \bar{u}_R^j i\not{D}_R u_R^j + \bar{d}_R^j i\not{D}_R d_R^j + \bar{L}^j i\not{D}_L L^j + \bar{e}_R^j i\not{D}_R e_R^j, \tag{1.4}$$

where a sum over j, the flavor (or generation) index, is assumed. One can quickly notices the difference between left-handed and right-handed components, in fact Q^j and L^j are the left handed quarks and leptons SU(2) doublets, written explicitly as

$$Q^j = \begin{pmatrix} u_L^j \\ d_L^j \end{pmatrix}, \qquad L^j = \begin{pmatrix} \nu_L^j \\ e_L^j \end{pmatrix}, \tag{1.5}$$

while u_R^j, d_R^j are the right-handed quark singlets and e_R^j is the right-handed charged-lepton singlets since in the SM neutrinos are considered only left-handed.

The $\not{D}$ term is the contracted form of $\gamma^\mu D_\mu$, in which γ^μ is the Dirac matrix and D_μ is the so called covariant derivative. $D_{R\mu}$ and $D_{L\mu}$ are needed so that the Lagrangian is invariant under SU(2) × U(1) local gauge transformations and differs between right- and left-handed fields

$$D_{L\mu} = \partial_\mu + igW_\mu^a \frac{\sigma^a}{2} + ig' \frac{Y}{2} B_\mu, \tag{1.6a}$$

$$D_{R\mu} = \partial_\mu + ig' \frac{Y}{2} B_\mu, \tag{1.6b}$$

where Y is the hypercharge of the filed on which D_μ operates, σ^a are the Pauli matrices and g and g' are the coupling constants.

Being SU(2) doublets, Q^j and L^j have weak isospin $T = 1/2$, with third components $T_3 = \pm 1/2$ for up- and down-quarks and neutral and charged leptons, respectively. On the other hand, right-handed fermions are SU(2) singlets therefore $T = 0$. Since the electromagnetic charge of a field can be written as a combination of hypercharge Y and weak isospin third component T_3,

$$Q = T_3 + \frac{Y}{2}, \tag{1.7}$$

one can easily compute the hypercharge value for all fermion knowing their third weak isospin component and electromagnetic charge, Table 1.1.

Fermion	T_3	Y	Q
u_L	1/2	1/3	2/3
d_L	-1/2	1/3	-1/3
u_R	0	4/3	2/3
d_R	0	-2/3	-1/3
ν_L	1/2	-1	0
e_L	-1/2	-1	-1
e_R	0	-2	-1

Table 1.1: values of the third component of weak isospin T_3, hypercharge Y and electromagnetic charge Q.

The third component of Eq. 1.1 depicts the Higgs field and its interactions with the gauge bosons [4] [5]

$$\begin{aligned} \mathcal{L}_H &= (D^\mu \phi^\dagger)(D_\mu \phi) - V(\phi^\dagger \phi) = \\ &= (D^\mu \phi^\dagger)(D_\mu \phi) - \Big(- \mu^2 \phi^\dagger \phi + \frac{\lambda^2}{2} (\phi^\dagger \phi)^2 \Big), \end{aligned} \tag{1.8}$$

the λ and μ are positive real parameters and ϕ is the SU(2) Higgs doublet whit hypercharge $Y = 1$, composed by an electromagnetic charged scalar field ϕ^+ and a neutral complex one ϕ^0

$$\phi = \begin{pmatrix} \phi^+ \\ \phi^0 \end{pmatrix}. \tag{1.9}$$

As for the fermion Lagrangian (1.3), the covariant derivative is needed to preserve invariance under SU(2) local gauge transformations, and having hypercharge 1 lead to a covariant derivative of the form

$$D_\mu = \partial_\mu + igW_\mu^a \frac{\sigma^a}{2} + \frac{1}{2} ig' B_\mu. \tag{1.10}$$

The Higgs potential reaches its minimum when $\phi^\dagger\phi = \mu^2/\lambda^2 \equiv v^2/2$, however this minimum is degenerate as there are infinite number of ground state if one considers $\mu^2 < 0$. Since each one of these minima has the same probability of being the actual ground state, one can arbitrarily choose one of them as the vacuum expectation value $\langle\phi_0\rangle = v/\sqrt{2}$. By choosing the ground state, SU(2)×U(1) symmetry of the Lagrangian is spontaneously broken and only one of the original 4 degrees of freedom of ϕ remain, the Higgs boson field $H(x)$ which is now real and scalar. Therefore, the Higgs doublet can be rewritten in the so called unitary gauge form

$$\phi = \frac{1}{\sqrt{2}}\begin{pmatrix} 0 \\ v + H(x) \end{pmatrix}. \tag{1.11}$$

By substituting Eq. 1.11 into Eq. 1.8 one obtains

$$-\frac{1}{8}g^2v^2(W^{+\mu}W^+_\mu + W^{-\mu}W^-_\mu) - \frac{1}{8}v^2(g^2 + g'^2)Z^\mu Z_\mu - \frac{1}{2}\lambda^2v^2H^2, \tag{1.12}$$

quadratic field object point out to the mass of the particle associated to that filed, hence it is clear from Eq. 1.12 that the gauge and H bosons have acquired mass

$$M_H = \lambda v, \tag{1.13a}$$

$$M_W = \frac{1}{2}gv, \tag{1.13b}$$

$$M_Z = \frac{1}{2}\sqrt{g^2 + g'^2 v}, \tag{1.13c}$$

$$M_\gamma = 0. \tag{1.13d}$$

Three of the gauge bosons $W^\pm$ and Z have acquired mass while the photon remained massless.

Lastly, the forth term in Eq. 1.1 pictures the Yukawa interactions between fermion fields and the Higgs field and it is responsible for the acquisition of mass by the fermions. It is written as

$$\mathcal{L}_Y = -\lambda^{ij}_d\bar{Q}^i\phi d^j_R - \lambda^{ij}_u\bar{Q}^i(i\sigma^2\phi)u^i_R - g^i_e\bar{L}^i\phi e^i_R + h.c., \tag{1.14}$$

in which a sum over i and j is assumed, g^i_e are coupling constants and $\lambda^{ij}_{d,u}$ are complex-variable matrices. Substituting Eq. 1.11 into the Yukawa Lagrangian (1.14) one finds

$$\mathcal{L}_Y = -\frac{v}{\sqrt{2}}\lambda^{ij}_\mu\bar{d}^i_L d^j_R - \frac{v}{\sqrt{2}}\lambda^{ij}_\mu\bar{u}^i_L u^j_R - \frac{v}{\sqrt{2}}g^i_e e^i_L e^i_R + h.c., \tag{1.15}$$

as for the gauge bosons, it stands clear that there is a mass term for e^i leptons, meaning electrons, muons and tauons, equal to

$$m_{e^i} = \frac{v}{\sqrt{2}} g^i. \tag{1.16}$$

From this dissertation, no term proportional to the neutrino field appear and that is why for many years it was believed to be massless. However, recent observations have confirmed that they do have masses and, moreover, that they mix among themselves generating the neutrino oscillations phenomenon [6, 7, 8, 9, 10, 11, 12]. According these studies, the flavor or weak eigenstates are a combination of the mass eigenstates following equation

$$\nu_L^i = \sum_j U_{ij} \nu_{m,L}^j, \tag{1.17}$$

where U is the Pontecorvo-Maki-Nakagawa-Sakata (PMNS) matrix, or neutrino mixing matrix, and characterises the weak charged-current in the lepton sector

$$\frac{g}{2\sqrt{2}} \bar{e}_L^i U_{ij} \gamma_\mu (1+\gamma_5) \nu_{m,L}^j W^{-\mu} + h.c. \tag{1.18}$$

U is the analogous to the quark mixing matrix which will be discussed in details in the upcoming section.

1.2 The Cabibbo-Kobayashi-Maskawa Matrix

Experimentally, the physical quarks observed are different from those defined as u^i and d^i fields in Eq 1.4. This is also supported by the quark mass terms in Eq. 1.15 where there is a $\bar{u}^i u^j$ terms for up-type quarks and a similar one for down-type quarks, instead of a term proportional to $\bar{u}^i u^i$. In order to find the mass eigenstates the solution is to diagonalize the λ^{ij} matrices introduced in Eq. 1.14. Thus, two new unitary matrices $S_{u,d}$ and $T_{u,d}$ are introduced such that

$$\lambda_{u,d} \lambda_{u,d}^\dagger = S_{u,d} D_{u,d}^2 S_{u,d}^\dagger, \tag{1.19a}$$

$$\lambda_{u,d}^\dagger \lambda_{u,d} = T_{u,d} D_{u,d}^2 T_{u,d}^\dagger, \tag{1.19b}$$

where $D_{u,d}$ are diagonal matrices. This leads to the definition

$$\lambda_{u,d} = S_{u,d} D_{u,d} T_{u,d}^\dagger. \tag{1.20}$$

The physical quark fields are now defined as: (the flavor eigenstates fields can now be written as the combination of mass eigenstates field)

$$u^i_L = S^{i,j}_u u^{j,phys}_L, \tag{1.21a}$$

$$u^i_R = T^{i,j}_R u^{j,phys}_R, \tag{1.21b}$$

$$d^i_L = S^{i,j}_L d^{j;phys}_L, \tag{1.21c}$$

$$d^i_R = T^{i,j}_R d^{j,phys}_R, \tag{1.21d}$$

and using these definitions in Eq. 1.15 one obtains

$$-\frac{v}{\sqrt{2}} D^{ii}_u \bar{u}^{i,phys} u^{i,phys} - \frac{v}{\sqrt{2}} D^{ii}_d \bar{d}^{i,phys} d^{i.phys}, \tag{1.22}$$

which have the same structure as the lepton mass quark term. It follows that the mass of a quark particle is:

$$m^i_{u,d} = \frac{v}{\sqrt{2}} D^{ii}_{u,d}. \tag{1.23}$$

The change from flavor to mass eigenstates can be done also in the interaction term of the Lagrangian (Eq. 1.4) in which it can be proven there are these terms:

$$-\frac{g}{\sqrt{2}}(J^{+\mu}W^+_\mu + J^{-\mu}W^-_\mu) - \frac{g}{\cos\theta_W} J^{N\mu} Z_\mu, \tag{1.24}$$

where the charged and neutral currents, $J^{\pm\mu}$ and $J^{N\mu}$, are defined as

$$J^{+\mu} = \bar{\nu}^a_L \gamma^\mu e^a_L + \bar{u}^a_L \gamma^\mu d^a_L, \tag{1.25a}$$

$$J^{-\mu} = h.c.(J^{+\mu}), \tag{1.25b}$$

$$J^{N\mu} = \sum_{a,f} \bar{f}^a \frac{\gamma^\mu}{2}[T_3 - (T_3 - 2\sin^2\theta_W Q)\gamma^5] f^a, \tag{1.25c}$$

in which f^a is a generic fermion filed of the a-th generation, Q is the electromagnetic charge and T_3 is the third weak isospin component. Since the diagonalizing matrices $S_{u,d}$ and $T_{u,d}$ are unitary by definition, the neutral current term (1.25c) remains unchanged. On the other hand, the charged current term (1.25a, 1.25b) involving quark fields can be written as

$$\bar{u}^{i,phys}_L (S^\dagger_u S_d)^{ij} \gamma^\mu d^{j,phys}_L. \tag{1.26}$$

The matrix $S^\dagger_u S_d \equiv V_{CKM}$ is called Cabibbo-Kobayashi-Maskawa matrix and depicts the mixing between the down-type quarks in charged-current interactions [13, 14].

The charged-current interaction Lagrangian can now be written in mass eigenstates basis as

$$\mathcal{L}_{cc,quarks} = -\frac{g}{\sqrt{2}} \begin{pmatrix} \bar{u}_L & \bar{c}_L & \bar{t}_L \end{pmatrix} \begin{pmatrix} V_{ud} & V_{us} & V_{ub} \\ V_{cd} & V_{cs} & V_{cb} \\ V_{td} & V_{ts} & V_{tb} \end{pmatrix} \gamma^\mu \begin{pmatrix} d_L \\ s_L \\ b_L \end{pmatrix} W_L^+ + h.c., \tag{1.27}$$

where the spinors represents the physical quark. Moreover, it comes foth that the charged weak interaction bosons, $W_\mu^\pm$, mediate the interaction between up-type and down-type quarks belonging to different families, hence quark flavor can change in weak interactions. Each element of V_{CKM} stands for the coupling strength coefficient between two quarks, meaning that, for example, the coupling between t and b with $|V_{tb}| \simeq 1$ is much stronger than that between u and b with $|V_{ub}| \simeq 0.004$.

The number of degrees of freedom of a $n \times n$ matrix is equal to n^2 therefore the V_{CKM} matrix has 9 degrees of freedom. However, looking at the Yukawa Lagrangian term

$$-m^i \bar{d}_L^{i,phys} d_R^{i,phys} - m^i \bar{u}_L^{i,phys} u_L^{i,phys}, \tag{1.28}$$

one can notice a left-over symmetry under U(1) transformations of the form

$$\begin{cases} u_L^i \to e^{i\alpha_i} u_L^i \\ u_R^i \to e^{i\alpha_i} u_R^i \end{cases} \qquad \begin{cases} d_L^i \to e^{i\alpha_i} d_L^i \\ d_R^i \to e^{i\alpha_i} d_R^i \end{cases}, \tag{1.29}$$

for a total of 6 parameters, $\bar{u}_L^i u_R^i$ and $\bar{d}_L^i d_R^i$ with $i = 1, 2, 3$, are invariant under U(1). This means that we can always use 5 of these U(1) symmetries to compute 5 parameters inside the V_{CKM} matrix reducing $N_{DoF} = 9 - 5$ leaving only 4 degrees of freedom. This allows for a parametrization of the V_{CKM} with 3 real mixing angles, $(\theta_{12}, \theta_{13}, \theta_{23})$ and 1 imaginary phase δ, responsible for the CP violation in weak interactions (covered later in Sec. 1.3). By defining $s_{ij} \equiv \sin\theta_{ij}$ and $c_{ij} \equiv \cos\theta_{ij}$, the V_{CKM} can be written as

$$V_{CKM} = \begin{pmatrix} c_{12}c_{13} & s_{12}c_{13} & s_{13}e^{-i\delta} \\ -s_{12}c_{23} - c_{12}s_{23}s_{13}e^{i\delta} & c_{12}c_{23} - s_{12}s_{23}s_{13}e^{i\delta} & s_{23}c_{13} \\ s_{12}s_{23} - c_{12}c_{23}s_{13}e^{i\delta} & -c_{12}s_{23} - s_{12}c_{23}s_{13}e^{i\delta} & c_{23}c_{13} \end{pmatrix} + \mathcal{O}(\lambda^4). \tag{1.30}$$

It is also possible to make explicit the hierarchy of the V_{CKM} elements using Wolfenstein parametrization [15], based on an expansion of the four parameters λ, the sine of the Cabibbo angle ($\lambda \simeq 0.226$), A, ρ and η, resulting in

$$V_{CKM} = \begin{pmatrix} 1 - \lambda^2/2 & \lambda & A\lambda^3(\rho - i\eta) \\ -\lambda & 1 - \lambda^2/2 & A\lambda^2 \\ A\lambda^3(1 - \rho - i\eta) & -A\lambda^2 & 1 \end{pmatrix} + \mathcal{O}(\lambda^4), \tag{1.31}$$

where

$$s_{12} = \lambda = \frac{|V_{us}|}{\sqrt{|V_{ud}|^2 + |V_{us}|^2}}, \tag{1.32a}$$

$$s_{23} = A\lambda^2 = \lambda|\frac{V_{cb}}{V_{us}}|, \tag{1.32b}$$

$$s_{13}e^{i\delta} = A\lambda^3(\rho + i\eta) = V_{ub}^*. \tag{1.32c}$$

Latest experimental measurements [16] estimate the magnitudes of the CKM matrix to be:

$$|V_{CKM}| = \begin{pmatrix} 0.97435 \pm 0.00016 & 0.22501 \pm 0.00068 & 0.003732^{+0.000090}_{-0.000085} \\ 0.22487 \pm 0.00068 & 0.97349 \pm 0.00016 & 0.04183^{+0.00079}_{-0.00069} \\ 0.00858\pm^{0.00019}_{0.00017} & 0.04111^{+0.00077}_{-0.00068} & 0.999118^{+0.000029}_{-0.000034} \end{pmatrix}. \tag{1.33}$$

1.3 Charge-Parity violation in the Standard Model

It particle physics, charge conjugation, C, is a mathematical operation which changes the electromagnetic charge of a particle into its opposite value, effectively transforming a particle into an antiparticle. An electrically neutral antiparticle may be identical to its corresponding particle. Parity, P, represents the reflection of the spatial coordinates through the origin. Parity conservation means that up, down, left and right are indistinguishable and, essentially, that the probability for a nucleus to emit a decay product along a given direction is the same for all other directions.

Strong interactions conserve C and P separately, thus conserving also CP, while weak interactions maximally violates both C and P and, minimally, also CP.

The CKM matrix can be parametrized with three real mixing angles and an imaginary phase, as discussed in Sec. 1.2. However, multiple parametrizations exists and they differ from each other by the position of the complex phase inside the matrix, which is not physically important. In fact, it is possible to define a CP-violation quantity which does not depend on the parametrization used. For example, the Jarlskog invariant, J_{CKM}, is defined using the following relation

$$\Im(V_{ij}V_{kl}V_{il}^*V_{kj}^*) = J_{CKM}\sum_{m,n=1}^{3}\epsilon_{ikm}\epsilon_{jln}, \qquad (i,j,k,l = 1,2,3), \tag{1.34}$$

and can be written as

$$J_{CKM} = s_{12}s_{13}s_{23}c_{12}c_{13}c_{23}^2 \sin\delta. \tag{1.35}$$

It can be shown that a necessary and sufficient condition for CP-violation to occur in the quark sector is:

$$(m_t^2 - m_c^2)(m_t^2 - m_u^2)(m_c^2 - m_u^2)(m_b^2 - m_s^2)(m_b^2 - m_d^2)(m_s^2 - m_d^2)J_{CKM} \neq 0. \qquad (1.36)$$

This equation establishes that for CP-violation not to exist any mass degeneracy between up-type quarks or down-type quarks must be absent, all three mixing angles must be different from 0 or 2π and the imaginary phase must be different from 0 or π. Eq 1.36 not only introduces limitations on the values of its elements but also on the number of quarks in the process. It is easy to see that if less than four different quarks are involved, then Eq. 1.36 would equal to 0. Therefore, there must be at least 4 different quarks inside a certain process in order to have CP-violation.

Considering a generic meson M and its CP conjugate $\overline{M}$, its final state f and its CP conjugate $\bar{f}$, one can define the following decay amplitudes:

$$A_f = \langle f|\mathcal{H}|M\rangle, \quad A_{\bar{f}} = \langle \bar{f}|\mathcal{H}|M\rangle, \quad \overline{A}_f = \langle f|\mathcal{H}|\overline{M}\rangle, \quad \overline{A}_{\bar{f}} = \langle \bar{f}|\mathcal{H}|\overline{M}\rangle, \qquad (1.37)$$

where $\mathcal{H}$ is the Hamiltonian. Inside these amplitudes two different phases can be characterized

$$A_f = |A|e^{i(\delta+\phi)}. \qquad (1.38)$$

The first, δ, is the *strong phase*, it represents the sum of all possible contributions from intermediate on-shell states in the decay process, usually a product of strong interactions, hence its name. Since strong interactions are CP-invariant, this phase does not change between A_f and $\overline{A}_{\bar{f}}$. The second, ϕ, is the *weak phase*, it arises from the coupling of the $W^{\pm}$ bosons and appears in its complex conjugate form in the CP-conjugate amplitude.

In a decay, the amplitude can be considered as the sum of all the contribution in the process:

$$A_f = \sum\nolimits_j |A_j|e^{i(\delta_j+\phi_j)}, \qquad (1.39)$$

where $|A_j|$ is the magnitude of the single elements in the process. CP-violation physically results in a difference between the final amplitudes $|A_f| \neq |\overline{A}_{\bar{f}}|$, possible only if at least two terms in the process have different strong and weak phases.

Considering the difference of the squared amplitudes, one obtains

$$|A_f|^2 - |\overline{A}_{\bar{f}}|^2 = -2\sum_{i\neq j}|A_i||A_j|\sin{(\delta_i - \delta_j)}\sin{(\phi_i - \phi_j)}. \qquad (1.40)$$

1.4 Neutral Meson

Concerning neutral mesons, CP violation phenomenology is enriched by an initial pure flavor eigenstate to potentially develop a component of the opposite flavor before decaying. This is possible because of the structure of the weak interaction which enables flavor mixing or oscillation, for example the $M^0 \leftrightarrow \overline{M}^0$ transition. There are four neutral mesons that can mix: K^0, D^0, B^0 and B^0_s.

Consider a state that is initially a superposition of $|M^0\rangle$ and $|\overline{M}^0\,\rangle$ as

$$|\psi(t=0)\rangle = a(0)|M^0\rangle + b(0)|\overline{M}^0\,\rangle. \tag{1.41}$$

In time, the state will evolve as

$$|\psi(t)\rangle = a(t)|M^0\rangle + b(t)|\overline{M}^0\,\rangle + \sum_i c_i(t)|f_i\rangle, \tag{1.42}$$

where f_i are all the possible final states. The two pure eigenstate define a subspace where the possible mixing states are described by the Shrödinger equation

$$i\frac{\partial}{\partial t}\begin{pmatrix} a(t) \\ b(t) \end{pmatrix} = \left(\mathbf{M} - \frac{i}{2}\mathbf{\Gamma}\right)\begin{pmatrix} a(t) \\ b(t) \end{pmatrix}, \tag{1.43}$$

in which $\mathbf{M}$ is the mass matrix and its elements are defined as follows:

$$M_{ij} = m_0\delta_{i,j} + \langle M_i|\mathcal{H}_{\mathrm{W}}|M_j\rangle + \sum_k \mathrm{P}\left(\frac{\langle M_i|\mathcal{H}_{\mathrm{W}}|f_k\rangle\langle f_k|\mathcal{H}_{\mathrm{W}}|M_j\rangle}{m_0 - E_{f_k}}\right), \tag{1.44}$$

and the element of the decay matrix are

$$\Gamma_{ij} = 2\pi\sum_k \delta(m_0 - E_{f_k})\langle M_i|\mathcal{H}_{\mathrm{W}}|f_k\rangle\langle f_k|\mathcal{H}_{\mathrm{W}}|M_j\rangle, \tag{1.45}$$

where $M_1 = M^0$, $M_2 = \overline{M}^0$, $\mathcal{H}_{\mathrm{W}}$ is the weak Hamiltonian and m_0 is the mass of the pure eigenstate M^0. The matrix $\mathbf{M}$ is associated with transitions via off-shell (dispersive) intermediate states, whereas $\mathbf{\Gamma}$ with on-shell (absorptive) intermediate states. if we expand the Shrödinger equations for both states of Eq. 1.43

$$i\frac{\partial}{\partial t}|M^0(t)\rangle = \left(\mathrm{M}_{11} - \frac{i}{2}\Gamma_{11}\right)|M^0(t)\rangle \;+ \left(\mathrm{M}_{12} - \frac{\mathrm{i}}{2}\Gamma_{12}\right)|\overline{M}^0(t)\rangle, \tag{1.46}$$

$$i\frac{\partial}{\partial t}|\overline{M}^0(t)\rangle = \left(\mathrm{M}_{21} - \frac{i}{2}\Gamma_{21}\right)|M^0(t)\rangle \;+ \left(\mathrm{M}_{22} - \frac{\mathrm{i}}{2}\Gamma_{22}\right)|\overline{M}^0(t)\rangle, \tag{1.47}$$

it is clear that off-diagonal term of **H** are related to flavor mixing transitions. Since the conservation of the CPT symmetry is required, it follows that $M_{11} = M_{22}$, $\Gamma_{11} = \Gamma_{22}$ and $M_{21} = M^*_{12}$, $\Gamma_{21} = \Gamma^*_{12}$. Therefore, one can write the mass-decay matrix as

$$\mathbf{H} = \begin{pmatrix} \mathrm{M} - \frac{\mathrm{i}}{2}\Gamma & \mathrm{M}_{12} - \frac{\mathrm{i}}{2}\Gamma_{12} \\ \mathrm{M}^*_{12} - \frac{\mathrm{i}}{2}\Gamma^*_{12} & \mathrm{M} - \frac{\mathrm{i}}{2}\Gamma \end{pmatrix}. \tag{1.48}$$

The eigenvalues of the mass-decay matrix are

$$\lambda_\pm = \mathrm{M} - \frac{\mathrm{i}}{2}\Gamma \pm \mathrm{F}, \tag{1.49}$$

with F being:

$$\mathrm{F} = \sqrt{\left(M_{12} - \frac{i}{2}\Gamma_{12}\right)\left(M^*_{12} - \frac{i}{2}\Gamma^*_{12}\right)} \tag{1.50}$$

Although small, the two eigenstates have a difference in mass values with which it is possible to label them as lower- and higher-mass eigenstate

$$\lambda_L^{(-)} = m_L - \frac{i}{2}\Gamma_L \equiv (M - \Re(F)) - \frac{i}{2}(\Gamma + 2\Im(F)), \tag{1.51a}$$

$$\lambda_H^{(+)} = m_H - \frac{i}{2}\Gamma_H \equiv (M + \Re(F)) - \frac{i}{2}(\Gamma - 2\Im(F)). \tag{1.51b}$$

The eigenvectors are

$$|M_H\rangle = p|M^0\rangle + q|\overline{M}^0\rangle, \tag{1.52a}$$

$$|M_L\rangle = p|M^0\rangle - q|\overline{M}^0\rangle, \tag{1.52b}$$

where p and q are complex parameters with $|p|^2 + |q|^2 = 1$ and their ratio is:

$$\frac{q}{p} = \sqrt{\frac{M^*_{12} - \frac{i}{2}\Gamma^*_{12}}{M_{12} - \frac{i}{2}\Gamma_{12}}}, \tag{1.53}$$

that can be used to rewrite the eigenvalues as

$$\lambda_{H,L} = M - \frac{i}{2}\Gamma \pm \frac{q}{p}\left(M_{12} - \frac{i}{2}\Gamma_{12}\right) \tag{1.54}$$

Using Eq. 1.52a, 1.52b one can write the pure M^0 and $\overline{M}^0$ states at time $t = 0$ as

$$|M^0\rangle = \frac{1}{2p}(|M_H\rangle + |M_L\rangle), \tag{1.55a}$$

$$|\overline{M}^0\rangle = \frac{1}{2q}(|M_H\rangle - |M_L\rangle), \tag{1.55b}$$

and since the time evolution of the $|M_L\rangle$ and $|M_H\rangle$ eigenstates are independent from one another, the time evolution of the two pure eigenstates will be

$$|M^0\rangle = \frac{1}{2p}\{e^{-im_Lt-\Gamma_L\frac{t}{2}}|M_L\rangle + e^{-im_Ht-\Gamma_H\frac{t}{2}}|M_H\rangle\}, \tag{1.56a}$$

$$|\overline{M}^0\rangle = \frac{1}{2q}\{e^{-im_Ht-\Gamma_H\frac{t}{2}}|M_H\rangle - e^{-im_Lt-\Gamma_L\frac{t}{2}}|M_L\rangle\}. \tag{1.56b}$$

The last step consist in substituting Eq. 1.52a, 1.52b into Eq. 1.56a, 1.56b in order to obtain an equation which describes the time evolution of a pure eigenstate:

$$|M^0(t)\rangle = g_+(t)|M^0\rangle + \frac{q}{p}g_-(t)|\overline{M}^0\rangle, \tag{1.57a}$$

$$|\overline{M}^0(t)\rangle = g_+(t)|\overline{M}^0\rangle + \frac{p}{q}g_-(t)|M^0\rangle, \tag{1.57b}$$

where

$$g_\pm = \frac{1}{2}\left(e^{-im_Ht-\frac{1}{2}\Gamma_Ht} \pm e^{-im_Lt-\frac{1}{2}\Gamma_Lt}\right). \tag{1.58}$$

Knowing the time evolution of a pure eigenstate, it is now possible to compute the decay rate of $|M^0\rangle$ into a final state f or $\bar{f}$. First considering the probabilities that a pure eigenstate has to go into one of those final states

$$A_f = \langle f|\mathrm{H}|M^0\rangle, \qquad \overline{A}_f = \langle f|\mathrm{H}|\overline{M}^0\rangle, \tag{1.59a}$$

$$A_{\bar{f}} = \langle \bar{f}|\mathrm{H}|M^0\rangle, \qquad \overline{A}_{\bar{f}} = \langle \bar{f}|\mathrm{H}|\overline{M}^0\rangle. \tag{1.59b}$$

Then introducing the following quantities

$$\lambda_f = \frac{q}{p}\frac{\overline{A}_f}{A_f}; \qquad \overline{\lambda_f} = \frac{1}{\lambda_f}; \qquad \lambda_{\bar{f}} = \frac{q}{p}\frac{\overline{A}_{\bar{f}}}{A_{\bar{f}}}, \qquad \overline{\lambda_{\bar{f}}} = \frac{1}{\lambda_{\bar{f}}}, \tag{1.60}$$

The decay rate of a meson M^0 into the final state f is:

$$\begin{aligned}\Gamma(t)_{M^0\to f} &= |\langle f|\mathrm{H}|M^0(t)\rangle|^2 = \\ &= |A_f|^2\left[|g_+(t)|^2 + |\lambda_f|^2|g_-(t)|^2 + 2\Re\{\lambda_f g_+^*(t)g_-(t)\}\right].\end{aligned} \tag{1.61}$$

Using now:

$$|g_\pm(t)|^2 = \frac{e^{-\Gamma t}}{2}\left[\cosh\left(\frac{\Delta\Gamma}{2}t\right) \pm \cos\left(\Delta m t\right)\right], \tag{1.62}$$

$$g_+^*(t)g_-(t) = \frac{e^{-\Gamma t}}{2}\left[\sinh\left(\frac{\Delta\Gamma}{2}t\right) - i\sin\left(\Delta m t\right)\right], \tag{1.63}$$

the decay rate becomes:

$$\begin{aligned}\Gamma(t)_{M^0\to f} = |A_f|^2\frac{e^{-\Gamma t}}{2}\Bigg[&(1+|\lambda_f|^2)\cosh\left(\frac{\Delta\Gamma}{2}t\right) + (1+|\lambda_f|^2)\cos\left(\Delta m t\right)\\ &+ 2\Re\{\lambda_f\}\sinh\left(\frac{\Delta\Gamma}{2}t\right) + 2\Im\{\lambda_f\}\sin\left(\Delta m t\right)\Bigg].\end{aligned} \tag{1.64}$$

In an analogous way, for $\overline{M}^0(t)$:

$$\begin{aligned}\Gamma(t)_{\overline{M}^0\to f} = |A_f|^2\left|\frac{p}{q}\right|^2\frac{e^{-\Gamma t}}{2}\Bigg[&(1+|\lambda_f|^2)\cosh\left(\frac{\Delta\Gamma}{2}t\right) - (1-|\lambda_f|^2)\cos\left(\Delta m t\right)\\ &+ 2\Re\{\lambda_f\}\sinh\left(\frac{\Delta\Gamma}{2}t\right) - 2\Im\{\lambda_f\}\sin\Delta m t\Bigg].\end{aligned} \tag{1.65}$$

In Eq. 1.64, since a decay rate of a $|M^0\rangle$ is considered, the terms proportional to $|A_f|^2$ are associated to decays occurring without oscillations while the terms proportional to $|\frac{q}{p}A_f|^2$ are the probability amplitudes for decays with oscillations. On the other hand, for the decay rate of a $|\overline{M}^0\rangle$ state the roles are swapped. The terms proportional to $|\overline{A}_f|^2$ regards decays without oscillations and those proportional to $|\frac{p}{q}A_f|^2$ represent oscillating decays. The decay rates into the $\bar{f}$ state can be obtained substituting $A_f \to A_{\bar{f}}$ in Eq. 1.64 and $\overline{A}_f \to \overline{A}_{\bar{f}}$ in Eq. 1.65.

The full time-integrated rates are obtained through the calculation of the integral $\int_0^\infty \Gamma_{M^0/\overline{M}^0(t)\to f}\Gamma e^{-\Gamma t}\mathrm{d}t$.

1.4.1 CP violation classification

Using the decay rates equations, one can classify CP violation in three different categories depending on the values of some terms inside the decay rates

1. CP violation in the decay.

   It is a time dependent observation and occurs when $|\frac{\overline{A}_{\bar{f}}}{A_f}| \neq 1$. This can happen either when $\Gamma_{M^0\to f} \neq \Gamma_{\overline{M}^0\to\bar{f}}$ or when $f = \bar{f}$. In this case, the CP asymmetry is defined as

   $$A_{CP}(f) = \frac{\Gamma(M\to f) - \Gamma(\overline{M}\to\bar{f})}{\Gamma(M\to f) + \Gamma(\overline{M}\to\bar{f})} = \frac{1-|\overline{A}_{\bar{f}}/A_f|^2}{1+|\overline{A}_{\bar{f}}/A_f|^2}. \tag{1.66}$$

   This is also the only possible contribution in a charged-meson decay.

2. CP violation in the mixing.

   It is observed when $P_{M^0\to\overline{M}^0} \neq P_{\overline{M}^0\to M^0}$ and the observable used is:

$$A_{CP} = \frac{P_{M^0\to\overline{M}^0} - P_{\overline{M}^0\to M^0}}{P_{M^0\to\overline{M}^0} + P_{\overline{M}^0\to M^0}}. \tag{1.67}$$

   However, because of the Eq. 1.57a and 1.57b one can write the probability of a meson to oscillate into its conjugate as

$$P_{M^0\to\overline{M}^0} = |\langle M^0|\overline{M}^0\rangle|^2 = \left|\frac{p}{q}\right|^2 |g_-(t)|^2, \tag{1.68a}$$

$$P_{\overline{M}^0\to M^0} = |\langle \overline{M}^0|M^0\rangle|^2 = \left|\frac{q}{p}\right|^2 |g_-(t)|^2, \tag{1.68b}$$

   thus reducing the observable to a simpler form

$$A_{CP} = \frac{\left|\frac{q}{p}\right|^2 |g_-(t)|^2 - \left|\frac{p}{q}\right|^2 |g_-(t)|^2}{\left|\frac{q}{p}\right|^2 |g_-(t)|^2 + \left|\frac{p}{q}\right|^2 |g_-(t)|^2} = \frac{\left|\frac{q}{p}\right|^2 - \left|\frac{p}{q}\right|^2}{\left|\frac{q}{p}\right|^2 + \left|\frac{p}{q}\right|^2}. \tag{1.69}$$

   It is therefore clear that CP violation in the mixing happens when $\left|\frac{q}{p}\right| \neq 1$.

3. CP violation in the interference between the mixing and the decay

   This type of CP violation happens when there is only one possible final state ($f = \bar{f}$) for both M^0 and $\overline{M}^0$. In such case, the neutral meson, for example M^0, can either decay straight to the final state or first oscillate into $\overline{M}^0$ and then decay to f. The same can be said for $\overline{M}^0$. If the decay rate of the second scenario between the two mesons is different ($\Gamma_{M^0\rightsquigarrow\overline{M}^0\to f} \neq \Gamma_{\overline{M}^0\rightsquigarrow M^0\to f}$) then there is CP violation. The observable used is

$$A_{CP}(t) = \frac{\Gamma_{M^0\to f}(t) - \Gamma_{\overline{M}^0\to f}(t)}{\Gamma_{M^0\to f}(t) + \Gamma_{\overline{M}^0\to f}(t)}. \tag{1.70}$$

   In order to ease notation three new terms are introduced

$$D_f = \frac{2\Re\{\lambda_f\}}{1+|\lambda_f|^2}; \qquad C_f = \frac{1-|\lambda_f|^2}{1+|\lambda_f|^2}; \qquad S_f = \frac{2\Im\{\lambda_f\}}{1+|\lambda_f|^2}. \tag{1.71a}$$

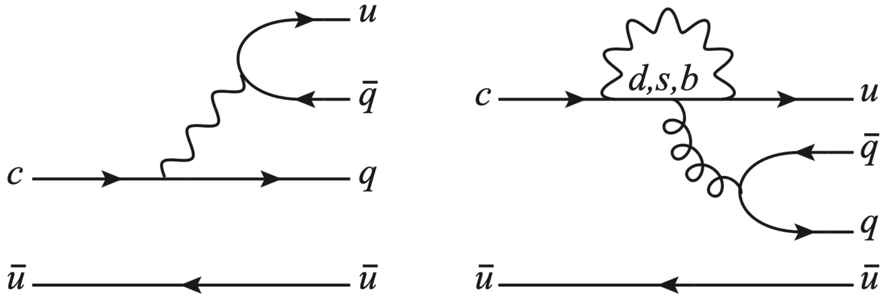

Figure 1.1: Examples of Feynman diagrams for charged two-body D^0 decays. Tree level on the left and one-loop penguin on the right.

With them Eq. 1.70 can be written as

$$A_{CP}(t) = \frac{C_f \cos(\Delta m t) + S_f \sin(\Delta m t)}{\cosh\left(\frac{\Delta\Gamma}{2} t\right) + D_f \sinh\left(\frac{\Delta\Gamma}{2} t\right)}, \tag{1.72}$$

where it is also assumed $\left|\frac{q}{p}\right| = 1$ to exclude the mixing between meson as a source of CP violation. In this case, $A_{CP}(t) \neq 0$ is possible only if one of the two terms in the nominator is $\neq 0$, therefore the possible sources of CP violation are

$$C_f \neq 0 \Longrightarrow |\lambda_f| \neq 1, \tag{1.73a}$$

$$S_f \neq 0 \Longrightarrow 2\Im\{\lambda_f\} \neq 0. \tag{1.73b}$$

Eq. 1.73a is the same condition for CP violation in the decay so, if one were to assume that no CP violation from the decay were possible and also from the mixing, since at the beginning of the computation it was assumed $\left|\frac{q}{p}\right| = 1$, then there would still be a possibility of CP violation occurring because of the interference between mixing and decay.

CP violation in the decay is usually referred to as *direct* while the other two types are called *indirect*.

1.5 CP violation in the charm sector

Neutral charm mesons are subject to the phenomenon of oscillation. They can freely go from a meson to an anti-meson, and vice versa, before decaying. This mechanism is called $D^0 - \overline{D}^0$ mixing and offers a grate opportunity for the study of CP violation. In fact, since D^0 decays into h^+h^- states through singly-Cabibbo-suppressed transitions, as shown in Fig. 1.1, the neutral charm meson system is the only one where the up sector quark takes part to the oscillation. Furthermore, because of this the tree-level Feynman diagrams of $D^0 \to h^+h^-$ decays involve the CKM matrix terms $V_{us}^* V_{cs}$ and $V_{ud}^* V_{cd}$. These terms, in Wolfenstein parametrization, correspond to $\mathcal{O}(\lambda^4)$, Eq. 1.31. To first order in the $D^0 - \overline{D}^0$ parameters, Eq. 1.66 can be written as

$$A_{CP}(f) = A_{CP}^{\text{dir}}(f) + A_{CP}^{\text{int}}(f). \tag{1.74}$$

Therefore, the effect of direct CP violation can be isolated defining the observable

$$\Delta A_{CP} = A_{CP}(K^+K^-) - A_{CP}(\pi^+\pi^-) = A_{CP}^{\text{dir}}(K^+K^-) - A_{CP}^{\text{dir}}(\pi^+\pi^-). \tag{1.75}$$

Due to the universality of indirect CP violation, a difference between the CP asymmetries of the two final states K^+K^- and $\pi^+\pi^-$, means that direct CP violation is present. It is also possible to expand Eq. 1.67 as a linear function of time

$$A_{CP}(f,t) = A_{CP}^{\text{dir}}(f) + \Gamma t A_{CP}^{\text{ind}}, \tag{1.76}$$

with $\Gamma = (\Gamma_H + \Gamma_L)/2$ being the average decay width. Introducing the parameter $A_\Gamma(f)$ as the asymmetry between the $D^0 \to f$ and $\overline{D}^0 \to f$ effective decay widths

$$A_\Gamma = \frac{\Gamma_{D^0 \to f} - \Gamma_{\overline{D}^0 \to f}}{\Gamma_{D^0 \to f} + \Gamma_{\overline{D}^0 \to f}} \simeq \frac{\Gamma_{D^0 \to f} - \Gamma_{\overline{D}^0 \to f}}{2\Gamma}, \tag{1.77}$$

Eq. 1.76 can be rewritten as

$$A_{CP}(f,t) = A_{CP}^{\text{dir}}(f) - \Gamma t A_\Gamma, \tag{1.78}$$

and so A_Γ is simply

$$A_\Gamma = -A_{CP}^{\text{ind}}. \tag{1.79}$$

Therefore, if a measurement report $A_\Gamma \neq 0$, it means that CP violation is present either in the mixing or in the interference between decay and mixing.

At the moment, the only observed CP violation is the direct one in the measurement of $\Delta A_{CP} = (-17.1 \pm 3.0 \pm 0.9) \cdot 10^{-4}$ [17], where the first error is statistical and the second is systematic.

Chapter 2

LHCb experiment

Between Run2 and Run3, the LHCb experiment faced its first upgrade, not only allowing the experiment to run at an instantaneous luminosity five times bigger than its last running period, but also to have a software only trigger. This new design is crucial for the reconstruction of events at maximum LHC interaction rate and their real-time selection. A complete renovation of the photon detection system RICH has been brought upon the detector, alongside the readout electronics of both calorimeter and muon systems.

2.1 Introduction

The LHCb experiment is one of the four large detectors at the Large Hadron Collider (LHC) accelerator at CERN. Initially the experiment was designed to study CP-violation and heavy-flavor hadrons decays through high precision measurements. However, it demonstrated excellent capabilities in a wider range of physics observable, thus becoming a general purpose experiment.

The LHCb Run 1-2 system would not allow for an increase in statistics even at higher luminosities, because of the limitations of the hardware trigger level, L0. The effect on hadronic decays is shown in the Fig. 2.1, where already at Run 2 luminosities the saturation of the signal yield is evident.

Moreover, inclusive flavor physics signal have relatively large cross section, and at the upgraded luminosity, each event in the LHCb acceptance will contain on average at least two long-lived hadrons not containing heavy quarks [19, 20]. This means that simple inclusive cut criteria would be either ineffective in the background rejection or would result in a downscaling of the signal, at high enough purity, as shown in the right panel in Fig. 2.1. With the objective in mind of running at a higher luminosity in

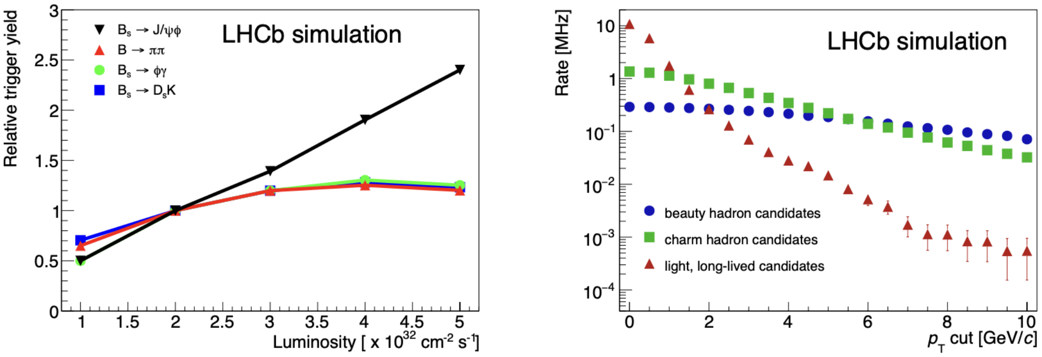

Figure 2.1: Left: relative trigger yield as a function of instantaneous luminosity, normalized to $\mathcal{L} = 2 \times 10^{32}$ cm^{-2}s^{-1}. Reproduced from [18]. Right: rate of decays reconstructed in the LHCb as a function of the cut in p_T of the decaying particle, for decay time $\tau > 0.2$ ps [19].

order to collect higher statistics, it became clear the necessity to remove L0 and shift to an all-software strategy able to discriminate signal channels based on the full event reconstruction.

With these premises, the LHCb upgraded detector was built with the aim of running at a nominal instantaneous luminosity of $\mathcal{L} = 2 \times 10^{33}$cm^{-2}s^{-1} and collecting events at the LHCb crossing rate of 40 MHz. The new all-software trigger is able to reconstruct in real time all events at the visible interaction rate of ~ 30 MHz.

The new trigger strategy, the higher luminosity and the consequently higher pile-up demanded a significant upgrade of the detector which brought a complete upgrade of the LHCb read-out electronics, now able to keep up with the 40 MHz bunch crossing rate. Also, the computing strategy had to be revised in order to deal with the expected increase in data volume.

2.2 LHCb Detector

2.2.1 Detector layout

The LHCb experiment is a single-arm forward spectrometer with a coverage of the pseudorapidity range $2 < \eta < 5$, located at the interaction point number 8 on the LHCb ring. In Fig. 2.2 the layout of the upgraded detector is shown. Throughout this thesis, the coordinate system used will have its origin at the nominal pp interaction point, the z axis will be along the beam pipe pointing at the muon system, the y axis pointing vertically upward and the x axis defining a right-handed system. The majority of the subdetectors are split into two mechanically independent parts, one half called *access side* or *Side A* at $x > 0$, and the other half called *cryogenic side* or *Side C* at $x < 0$. This is done for an easier access at the beam pipe and maintenance purpose. Notably, the only subsystems without this property are the two Cherenkov detectors.

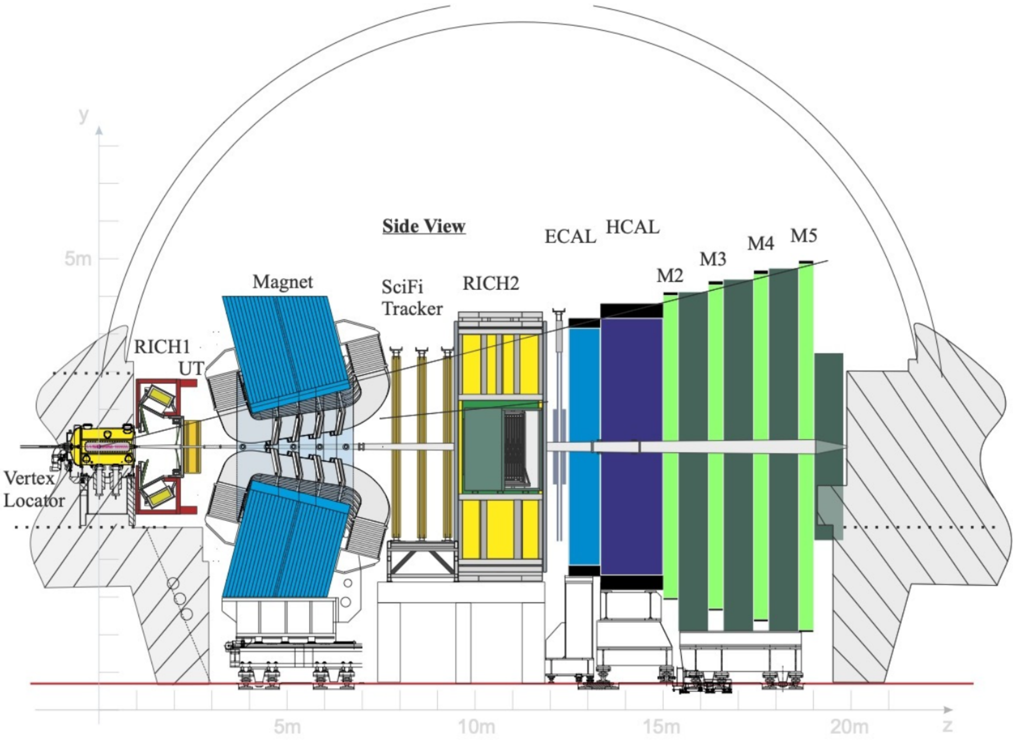

Figure 2.2: Upgraded LHCb experiment layout.

The first component met by the particles is the so called vertex locator (VELO), an array of pixel silicon detectors which surround the interaction region, after that there is the silicon-strip upstream tracker (UT) followed by the large-aperture dipole magnet. After the magnet one finds the three scintillating fibre tracking (SciFi Tracker) stations, used in the downstream region in the original LHCb experiment.

The particle identification (PID) portion is comprised of two ring imaging Cherenkov detectors (RICH1 and RICH2) working with C_4F_{10} and CF_4 gases as radiators, an electromagnetic calorimeter (ECAL) of the shashlik-type, an hadronic calorimeter (HCAL) which uses an iron-scintillator tile sampling mechanism and four stations of muon chambers (M2-5) interleaved with iron shielding. Because of the new all software trigger the Scintillating Pad Detector, the Pre-Shower and the most upstream muon station lost most of their usefulness and therefore were removed.

2.2.2 The magnet

The dipole magnet remains unchanged with respect of Run 1-2. It is composed of two identical saddle-shape coils, mounted symmetrically inside a window-framed yoke. Each coil is made of five triplets of aluminium pancakes and is supported by cast aluminium clamps fixed to the yoke. In order to match the detector acceptance the pole gap increases both horizontally and vertically in the direction of the downstream tracking stations.

The magnet is designed to provide a vertical magnetic field with a bending power of $\simeq 4$ Tm. During data taking, the magnet polarity is reversed regularly every few weeks, with the goal of obtaining a roughly equal data size for both magnetic field configurations.

2.3 Vertex Locator

The VELO is able to look directly at the beam collision region and see track of ionising particles produced. With this ability, it can measure the location of interaction vertices, of displaced vertices and the distance between them. The vertex locator informations are directly used by the reconstruction algorithm, providing discrimination knowledge for the subsequent event selection. The apparatus has been redesigned [21] in order to cope with the increased luminosity and the trigger-less 40 MHz readout requirement of the upgraded experiment. The technology of the new version of VELO is pixelated hybrid silicon detectors, arranged in modules and cooled via a silicon microchannel cooler. The principal vacuum vessel and motion services structures remain constant from the Run 1-2 version, while the RF Boxes, closed spaces that separate the detector with the particle beam, are entirely redesigned, reducing both materials needed and the inner radius of the VELO along the beam line. A new structure, called storage cell, is added directly upstream of the VELO inside the beam vacuum.

The principal quantity that the detector must be able to obtain is the impact parameter resolution σ_{IP}, that is the precision with which the perpendicular distance of a track to a point is measured. The parameters this quantity depends on are: the track transverse-momentum, p_{T}, the average axial distance between the material and the second measurement, r_1, the distances between the first and second measurements, Δ_i ($i = 1, 2$), and the position uncertainties of those measurements, σ_i. In case of the

VELO, the impact parameter resolution can be approximated as [22]:

$$\sigma_{\mathrm{IP}}^2 \approx \left(\frac{r_1}{p_T[\mathrm{GeV/c}]}\right)\left(0.0136\ [\mathrm{GeV/c}]\sqrt{\frac{x}{X_0}}\left(1+0.038\ \ln\frac{x}{X_0}\right)\right)^2 + \frac{\Delta_2^2\sigma_1^2+\Delta_1^2\sigma_2^2}{\Delta_{12}^2}, \tag{2.1}$$

where x/X_0 is the fraction of radiation length traversed before the second measurement. Equation 2.1 can be divided in two terms. The first takes into account the possible multiple scatterings along the path and establishes an assessment of the measure degradation. The second term is the extrapolation error due to the detector and it is highly dependant of the apparatus geometry. The upgraded VELO primary objective was to achieve a performance at least as good as that of its predecessor in both σ_{IP} and track-finding efficiency given the upgraded instantaneous luminosity.

The detector consists of a series of identical modules placed perpendicular to the beam line, filled with pixelated ASICs. The modules distribution must cover the full pseudorapidity acceptance of LHCb ($2 < \eta < 5$) as well as ensure that most tracks from the interaction region traverse at least four pixel sensors. The necessary number of modules to fulfil these requirements is 52, shown in Fig. 2.3, including the modules placed upstream of the interaction region with which the unbiased measurement of the primary vertices is improved.

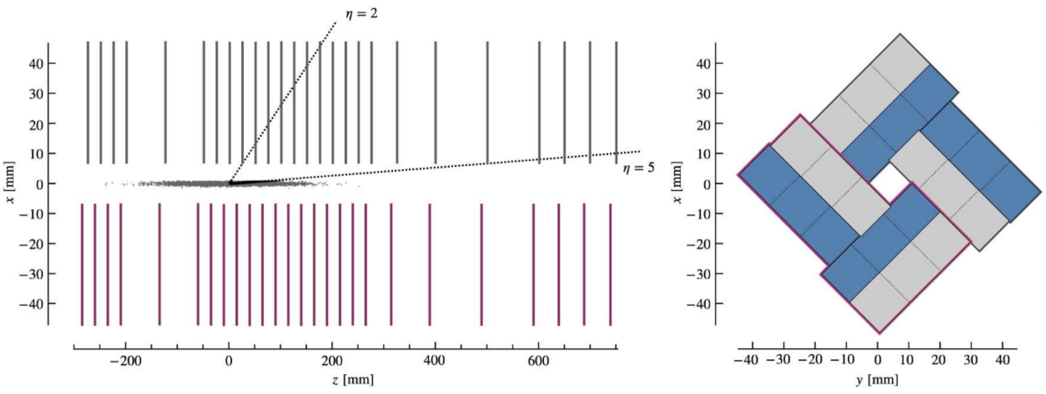

Figure 2.3: Left: top view of the zx plane at $y = 0$ of the modules inside the VELO, in addition an illustration of the nominal LHCb pseudorapidity acceptance, $2 < \eta < 5$. Right: view of the xy plane at one side of the VELO detector showing the nominal layout of the ASICs around the z axis. Half of them are placed on the upstream module face (grey), half of them on te downstream module face (blue). The modules highlighted in purple are on the Slide C.

The modules are arranged with a 25 mm distance between them and are divided into two halves, Slide C and Slide A. The two slides are practically identical, the only difference being a minor displacement of modules from Slide A by +12.5 mm in z, to ensure overlap between the modules once the apparatus is closed. This guarantee full azimuthal coverage. The square pixel detectors are organized as a 45° rotated 'L' shape, as shown in figure 2.3, only for structural reasons.

2.4 Upstream Tracker

Commonly referred as UT, it is located between the RICH1 detector and the dipole magnet. Its duty is charged-particle tracking and, since it is one of the first detectors met by the shower, the information gathered are vital for the first processing algorithm of the experiment [20]. Combining the UT hits and the VELO tracks, a first determination of the track momentum p can be made with a moderate precision of ($\sim$ 15%). An important feature of the Upstream Tracker is the ability to give a momentum and charged estimate only for tracks with $p_{\mathrm{T}} > 0.2\mathrm{GeV/c}$, because it speeds up the matching algorithm with the SciFi Tracker hits. Moreover, the UT significantly reduces the rate of fake tracks created by possible mismatched VELO and and SciFi Tracker segments. Lastly, the UT is able to detect an measure particles that decay after the VELO, e.g. long lived K^0_S and Λ particles.

A silicon microstrip technology was chosen to build the detector. The detector has a role to fulfil in the trigger algorithm and needs to be effective in suppressing fake tracks, therefore its acceptance must have no gaps. Concurrently, the detector must have a single-hit efficiency high enough to ensure that at least 99% of charged particles leave a hit in at least three planes, while having a hit purity capable of minimising spurious hits due to noise. The detector should keep an occupancy below few percent across all its surface. For this to happen, the radial dependence of charged-particles density has been taken into account and the detector segmentation was made finer near the beam pipe.

One of the objective of the redesign was to significantly reduce the overall material used in the forward region of acceptance compared to Run 1-2.

The UT detector is made of four planes of silicon detectors organised in two stations, Fig. 2.4. At the center, the circular hole provides clearance for the beam pipe. The arrangement and design of the sensors in the UT detector keep the maximum occupancy below 1%.

The silicon sensor, shown as coloured boxes in the image, are arranged in vertical units called *staves*. A stave provides mechanical support for the sensor and the FE electronics, as well as active cooling in the form of evaporative CO_2.

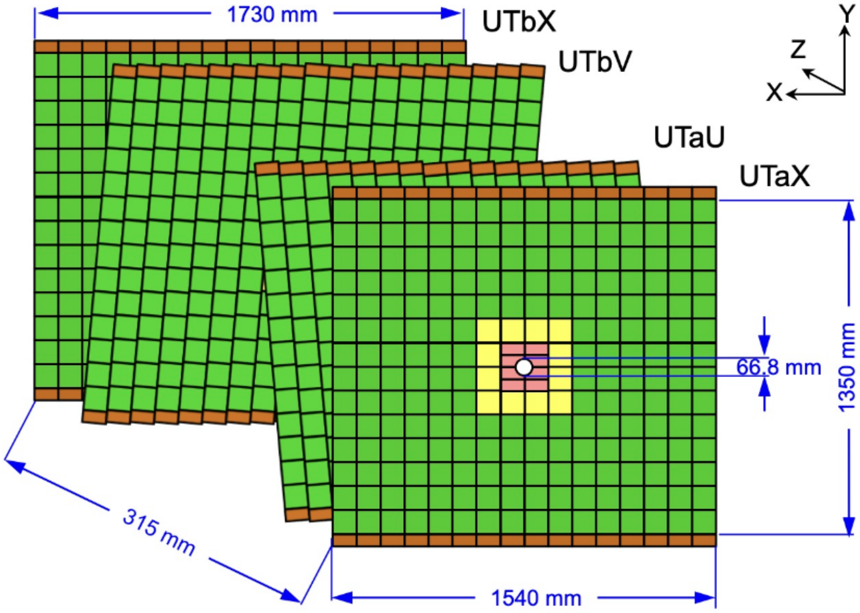

Figure 2.4: Geometry layout of the four UT silicon planes. Different colour designate different sensors: green for Type-A, yellow for Type-B, pink for Type-C and Type-D

The first station, labelled ’a’, comprises an x-measuring layer (UTaX) with vertical strips and a stereo layer (UTaU) with strips inclined by 5°, both made of 16 staves each. The second station, ’b’, is similar but has first a stereo layer (UTbV) with the opposite inclination with respect to the one in station ’a’,then a vertical layer with vertical strips (UTbX). Both layers contains 18 staves each. The two pairs are symmetrically positioned around $z = 2485$ mm, with a gap between UTaU and UTbV of 205 mm, and of 55 mm between the two layers of each station.

2.5 Scintillating fibre tracker

Also referred to as SciFi tracker, it is positioned after the dipole magnet. Its role is charged-particle tracking and momentum measurement. In particular, the objective for this detector is to achieve momentum resolution and tracking efficiency for b- and c-hadrons at least comparable with those obtained during Run 1 and Run 2, but with the higher particle density of the upgraded experiment.

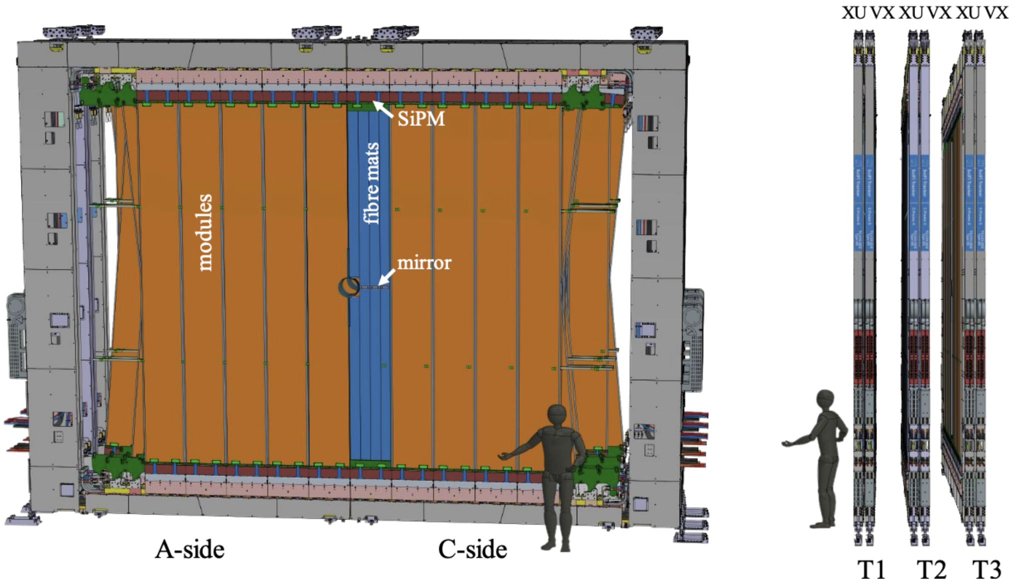

Figure 2.5: Front and side views of a 3D model of the SciFi tracker detector

The design of the detector must guarantee a single hit position resolution better than 100 μm in the magnet binding plane all the while maintaining an hit reconstruction efficiency better than 99%. Because the position resolution is the primary objective of the detector, it is necessary a good rigidity of the mechanical apparatus itself. The position of the detector elements must be stable within a precision of 50 μm along x and 300 μm along z. Moreover, the detector elements should be straight along their length within 50μm. In order to minimise additional multiple scattering and secondary particle production, the material used for the SciFi tracker has been reduced such that each of the 12 layers should not introduce more than 1% of radiation length. With these requirements in mind, the technology chosen to build the tracker with was scintillating fibre, hence the name SciFi.

The Detector comprises 12 detection planes in total arranged in 3 stations (T1, T2, T3), each with 4 layers in an X - U - V - X configuration, Fig. 2.5. Each plane has multilayered fibre mats of 250 μm diameter plastic scintillating fibres. The detector acceptance spans a range that goes from 20 mm, near the beam pipe, up to 3186 mm horizontally to the left and to the right of the beam pipe, and up to 2425 mm vertically both upward and downward. Each station has its own C-Frame, with which it can be moved independently from the other stations. All stations are built using the same SciFi modules which is 52 cm wide and span the full vertical length, except for a few modules

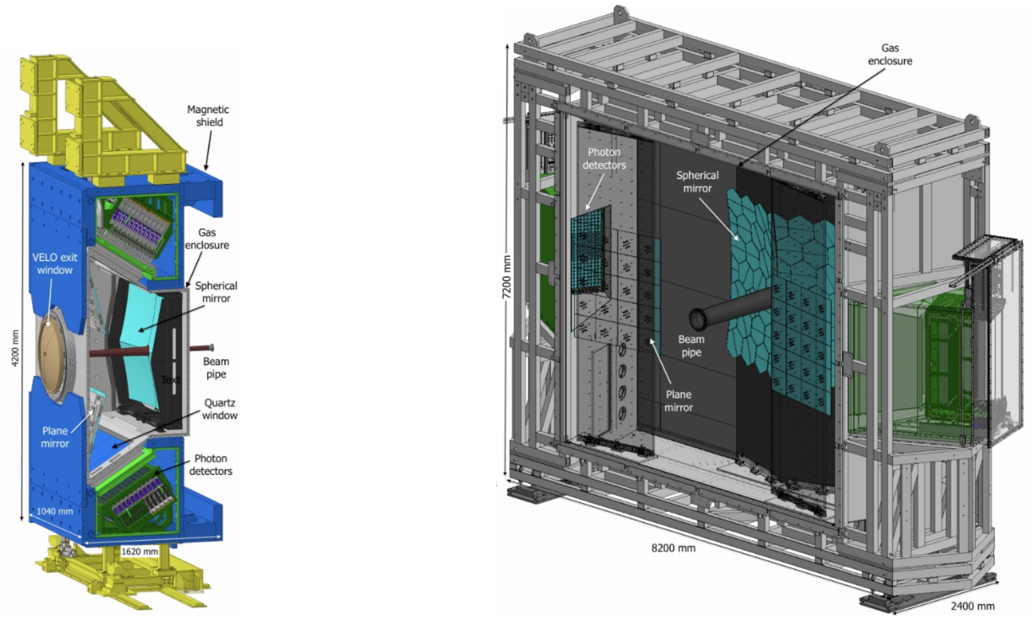

Figure 2.6: 3D view of the RICH1 (left) and RICH2 (right) detectors.

near the beam pipe. Each module is composed of eight fibres mats and are all identical with the exception of the modules near the beam pipe. The optical signal emitted by the fibres is collected by a total of 524200 silicon phonon multiplier (SiPM) channels organized into 4096 128-channel arrays.

2.6 RICH detector

The Ring-Imaging Cherenkov (RICH) detector plays a vital role in the LHCb experiment since it provides hadrons particle identification in the range of $2.6 - 100$ GeV/c momentum range. In particular it provides a way to identifies topologies that would otherwise be identical, e.g. $B^0_{(s)} \to \pi^+\pi^-, K^+K^-$ decay modes. Also it heavily reduces combinatorial background in decay modes involving hadrons in the final state, for example $B^0_s \to \phi\phi$, where $\phi \to K^+K^-$. Moreover, it allows to perform the flavor tagging of a $B^0_{(s)}$ meson directly at the production vertex using charged kaon identification from the $b \to c \to s$ decay chain.

The system is divided in two detectors, RICH1 and RICH2 shown in Fig. 2.6. The first is positioned before the dipole magnet, its photon detector planes are positioned above and below the beam pipe. The apparatus covers an angular acceptance of 25-300 mrad in the magnet bending plane and 25-250 mrad in the vertical plane. It uses C_4F_{10} gas radiator with a refractive index of $n = 1.0014$ which, at standard temperature and pressure (STP), produces Cherenkov radiation with wavelength $\lambda = 400$ nm. This allows to perform particle identification in the momentum range from 2.6 to 60 GeV/c. The RICH2 is instead located after the dipole magnet and has its detector planes on the sides of the beam pipe. The acceptance in this case is of 15-120 mrad in the magnet bending plane and 15-100 mrad in the vertical direction. The detector is designed to provide particle identification for higher momentum articles, from 15 to 100 GeV/c. It works with CF_4 as gas radiator which has an $n = 1.005$ and produces Cherenkov radiation of $\lambda = 400$ nm at STP.

With the increase of instantaneous luminosity the detector must be able to read the increased quantity of events but in the same time interval as the previous runs. This forces an increase in the read out rate of the detector up to 40 MHz, which is the rate of events corresponding to the new experiment nominal instantaneous luminosity. The RICH system photon detection chain has been completely substituted, since the former hybrid photon detector (HPD) [23] had embedded front-end electronics limited to a 1 MHz output rate. The HPDs have been replaced with multi-anode photomultiplier tubes (MaPMTs) equipped with new FE electronics, described in section **??**.

2.7 Trigger and real-time analysis

The trigger system is responsible of selecting events that are physically interesting in the midst of all the events registered by the detectors. Its primary goal is to reduce the data volume. With the upgraded instantaneous luminosity in *pp* collisions, it can reach 4 TB/s something wich is not sustainable both economically and on term of space to save all this data on. Therefore, the trigger system has the objective of reducing data volume down to 10 GB/s, that can then be recorded to a permanent offline data storage. Because of the staggering number of bunch crossings which may contain interesting physics phenomena, a simple traditional trigger strategy which uses a small set of generic signatures, would not be effective.

Instead, LHCb uses a *real-time analysis* approach, already used during Run 2 [24]. It consists of a full reconstruction and identification of the signal of interest, with only a limited subset of information saved regarding the rest of the event. This approach is then followed by a full offline quality reconstruction. The trigger system is divided into two stages: the HLT1, an high level trigger which reduces the volume bay a factor of 20, and the HLT2, responsible for the full offline quality reconstruction and selection.

Between the two trigger stages a disk buffer of about 30 PB is used to park the data while performing the alignment and calibration of the detectors in real-time.

2.7.1 HLT1

As already mentioned, this trigger stage has the primary goal to reduce the data volume and therefore the event rate. However, this has to be achieved while maintaining a good efficiency across the whole LHCb physics programme. An important consideration is that the signal rates are dominated by charm and beauty hadron decays which can be reconstructed within the LHCb acceptance. Other signals that are interesting for LHCb, such as electroweak or quarkonia, are significantly lower.

With such a high signal rate, it is important for HLT1 to select only events containing real signal while getting rid off fake tracks or random combinations of tracks. If so, at a luminosity of $2 \times 10^{33}\mathrm{cm}^{-2}\mathrm{s}^{-1}$, HLT1 system could maintain ~ 1 MHz output rate to satisfy the requirements for the full LHCb physics programme.

The satisfaction of the above-mentioned requirements has the natural outcome the ability of HLT1 to reconstruct and select these physics signatures:

- Tracks or two-track vertices displaced from the primary *pp* interaction (PV). The importance of this signature comes from the ability to select any event having at least a long-lived-hadron or τ lepton. This covers almost all LHCb analyses.
- Leptons, most importantly muons, no matter how displaced from the PV.

These physics constraints define the requirements on the track reconstruction system which are the following:

- HLT1 must be able to reconstruct all tracks in the VELO acceptance. This will precisely identify the primary vertices and will enable to compute the displacement of other tracks or secondary vertices.
- the trigger system must be able to reconstruct tracks whether they are displaced or not.
- its reconstructed track momenta must be precise at percent level.
- HLT1 must provide an accurate and precise covariant matrix of the tracks near the beam line.
- has to recognize tracks as leptons or non-leptons.

Depending on the physics that one want to probe, there is a kinematic threshold above which the trigger must be able to work efficiently. In the case of the charm and beauty programme, the experiences of Run 1 and 2 established that a p_{T} of 500 MeV as threshold is sufficient. However, for strange hadron it would be best to re construct track with a p_{T} as low as possible. A more general requirement would be the ability to reconstruct tracks with a momentum of 3 GeV, corresponding to the lowest momentum at which is possible to identify muons in LHCb.

2.7.2 HLT2

The second level trigger takes the information provided by the HLT1 and the consequent real-time alignment and calibration of the detector to perform an offline-quality reconstruction. If an event satisfies the requirements of this part of the trigger, it is recorded in the permanent storage.

The system must be able to perform the offline-quality reconstruction on all the events, using also the real-time alignment and calibration, and must be able to support an order of 3000 individual selection algorithms for the selection of interesting signals. In order for this to happen, the reconstruction is dived into four parts: charged particle pattern recognition, calorimeter reconstruction, particle identification and Kalman fit of reconstructed tracks, the last used to reach the best precision and accuracy for the parameters of the tracks.

The different selection algorithms are each designed for a particular signal topology and/or physics analysis. Each selection algorithm not only determine which event to record on the permanent storage, but also a subset of data relative to that event. This *real-time analysis*, called `Turbo`, allows for the rate of recorded events to be increased by decreasing the number of information recorded for each event. The `Turbo` mechanism, already used in Run 2 [25][24], leaves the possibility to save any amount of information on the event that is stored, from the lowest possible of two tracks and vertex coordinates for a two-body decay, up to the full event information. This decision depends on the kind of physics channel under study [26]. Still with the objective of minimizing overall data volume, the selections of HLT2 are grouped into *streams*, with each string having informations regarding a specific physics logic. For this reason, streams are configured according to the physics channel they belong to, e.g. charm physics, hadronic beauty decays etc.

Chapter 3

Data analysis and fit strategy

This chapter presents the analysis strategy for the measurement of $\Delta A_{CP} \equiv A_{CP}(D^0 \to K^+K^-) - A_{CP}(D^0 \to \pi^+\pi^-)$.

3.1 Analysis strategy

The raw asymmetry of D^0 decays to a CP eigenstate f is defined as

$$A_{\text{raw}}(f) = \frac{N(D^0 \to f) - N(\overline{D}^0 \to f)}{N(D^0 \to f) + N(\overline{D}^0 \to f)}, \tag{3.1}$$

where $N(D^0 \to f)$ and $N(\overline{D}^0 \to f)$ are the signal yields of D^0 and $\overline{D}^0$ mesons decaying into the final state f. The two possible final states K^+K^- and $\pi^+\pi^-$ are CP eigenstates, meaning that it is not possible to deduce the flavor of the starting meson from its decay products. A solution consists in looking at the particles produced in the same decay as $D^0(\overline{D}^0)$, using the technique called *taste tagging.* There are two ways of performing flavor tagging, *prompt* and *semileptonic.* In this study, only the first one has been used.

Prompt tagging consists of looking at the charge of the pion produced in the $D^{*\pm}$ decays. In fact, D^{*+} decays to $D^0\pi^+$, while D^{*-} to $\overline{D}^0\pi^-$ so π^+ will identify D^0, while π^- will identify $\overline{D}^0$. The $D^{*\pm}$ mesons are produced promptly from *pp* collisions, hence the name *prompt tagging.*

The raw asymmetry defined in Eq. 3.1 is not directly equal to the physical CP asymmetry defined in Eq. 1.66, due to the presence of nuisance asymmetries. One would be due to the detector response not being perfectly symmetric, causing a difference between the cross-section of particles and antiparticles. This detection asymmetry for the hadron

h^+ can be written as

$$A_{\mathrm{D}}(h^+) = \frac{\varepsilon(h^+) - \varepsilon(h^-)}{\varepsilon(h^+) + \varepsilon(h^-)}, \tag{3.2}$$

where $\varepsilon(h^{\pm})$ is the reconstruction efficiency of the $h^{\pm}$ hadron integrated over its momentum distribution. Another asymmetry would be related to the different production rates of D^0 and $\overline{D}^0$, defined as

$$A_{\mathrm{P}}(D^0) = \frac{\sigma(D^0) - \sigma(\overline{D}^0)}{\sigma(D^0) + \sigma(\overline{D}^0)}, \tag{3.3}$$

with $\sigma(D^0)$ and $\sigma(\overline{D}^0)$ being the inclusive production cross-sections of D^0 and $\overline{D}^0$ in pp collisions. In the case of D^0 mesons produced by D^* mesons, the production asymmetry $A_{\mathrm{P}}(D^0)$ is equal to $A_{\mathrm{P}}(D^{*+})$. Also, the number of reconstructed D^0 and $\overline{D}^0$ candidates with the prompt tag is proportional to the reconstruction efficiencies, the production rates and the branching fractions

$$N(D^0 \to f) \propto \sigma(D^{*+})\varepsilon(\pi^+)\Gamma(D^0 \to f) \tag{3.4a}$$

$$N(\overline{D}^0 \to f) \propto \sigma(D^{*-})\varepsilon(\pi^-)\Gamma(\overline{D}^0 \to f) \tag{3.4b}$$

therefore, using Eq. 1.66, 3.2, 3.3 and 3.4 the raw asymmetry defined in Eq. 3.1 can be written as

$$A_{\mathrm{raw}} = \frac{A_{CP}(f) + A_{\mathrm{P}}(D^{*+}) + A_{\mathrm{D}}(\pi^+) + A_{CP}(f)A_{\mathrm{P}}(D^{*+})A_{\mathrm{D}}(\pi^+)}{1 + A_{\mathrm{P}}(D^{*+})A_{CP}(f) + A_{\mathrm{P}}(D^{*+})A_{\mathrm{D}}(\pi^+) + A_{CP}(f)A_{\mathrm{D}}(\pi^+)}. \tag{3.5}$$

Since the production asymmetry value is expected to be of the order of 1% [27] and the detection asymmetry is of the same order, Eq. 3.5 can be simplified up to $\mathcal{O}(10^{-6})$ as

$$A_{\mathrm{raw}}(f) = A_{CP}(f) + A_{\mathrm{P}}(D^{*+}) + A_{\mathrm{D}}(\pi^+). \tag{3.6}$$

As a consequence, the difference between the two raw asymmetries is equal to the difference between the CP asymmetries

$$\Delta A_{\mathrm{raw}} = A_{\mathrm{raw}}(K^+K^-) - A_{\mathrm{raw}}(\pi^+\pi^-) = A_{CP}(K^+K^-) - A_{CP}(\pi^+\pi^-) = \Delta A_{CP}. \tag{3.7}$$

This is possible because production and detection asymmetries are independent of the final state. Even so they vary as a function of the kinematics, meaning that if the kinematic distribution differs between the reconstructed $D^0 \to K^+K^-$ and $D^0 \to \pi^+\pi^-$ decays, then these nuisance asymmetries may not cancel off completely. To avoid possible residual effects, a weighting technique is used to equalize relevant kinematics distributions.

3.2 Data sample and selection

For this analysis we used a subset of the *pp*-collision data of LHCb, taken in 2024 at a centre of mass energy of $\sqrt{s} = 13.6$ TeV. Data have been divided in 9 blocks according to changing data-taking conditions, related to various version of the detector alignment, magnet polarity and detector conditions. Candidates are first selected online through an exclusive HLT2 trigger lines in the Turbo stream, which select the D^* decay chain relevant for this analysis:

- `Hlt2Charm_DstpToD0Pip_D0ToKmKp`;
- `Hlt2Charm_DstpToD0Pip_D0ToPimPip`.

Additional requests are also applied at the HLT1 level of the trigger, to further clean the events from the background

- `D0_Hlt1TrackMVADecision_TOS`: it looks for a single track with good reconstruction quality, high p_T and significant IP with respect to the PV;
- `D0_Hlt1TwoTrackMVADecision_TOS`: it looks for couples of long tracks which are both characterised by good reconstruction quality and high momentum, and are consistent with the decay of a high p_T particle significantly displaced from the PV;
- `D0_Hlt1D2PiPi,KKDecision_TOS`: this exclusive line was introduced in Run 3 and has the ability to select charm decays with relatively high purity.

The triggered data were subjected to an additional offline selection, summarized in Table 3.1. These requirements are based on:

- $m(D^0\pi)$: the invariant mass to select the signal region;
- χ^2_{IP}: the impact parameter (IP) is the minimum distance between the reconstructed track and the primary vertex. It is useful to distinguish between particles coming from the primary vertex or short-lived resonances, and daughter particles coming from long-lived particles like D mesons. On average, a D daughter particle has a larger IP than a particle produced at the primary interaction. Usually the χ^2 of this parameter (IPχ^2), defined as the increase in the vertex-fit χ^2 when including this track, shows a better separation than the IP itself;
- DLL$_{K\pi}$: the discriminating variable for the particle identification is the so called $\Delta \log \mathcal{L}$ (DLL). The pion mass hypothesis is taken as a reference and the discrimination between the mass hypotheses is performed exploiting the difference of the

likelihood logarithm under a generic hypothesis and the pion hypothesis. In this way the DLL for the pion hypothesis is always zero. In particular the variables used in this analysis are the $\mathrm{DLL}_{K\pi}$, that is the difference between the logarithm of the likelihood under the K hypothesis and under the π hypothesis.

- It is also important to cut kinematic regions where a large soft-pion asymmetry is detected, since the expansion of A_{raw} described in Sec. 3.1 is valid only for low asymmetry values. For this reason only kinematic regions with asymmetries lower than 1% are kept. The fiducial cuts used for this purpose are defined as

$$|p_x(\pi_s)| < \alpha(p_z(\pi_s) - p_0) \quad \text{AND} \tag{3.8}$$

$$|p_y(\pi_s)/p_z(\pi_s)| < 0.2 \quad \text{OR} \quad |p_x(\pi_s)| > p_1 - \beta_1 p_z(\pi_s) \quad \text{OR} \quad |p_x(\pi_s)| > p_2 + \beta_2 p_z(\pi_s), \tag{3.9}$$

  where $\alpha = 0.317$, $p_0 = 2400$ MeV/c, $p_1 = 418$ MeV/c, $p_2 = 497$ MeV/c, $\beta_1 = 0.01397$ and $\beta_2 = 0.01605$.

There are also two new requirements with respect to Run 2:

- the request on the "radius" of the vertex defined as

$$R_{xy} = \sqrt{(\mathrm{END\_VTX\_Y}(D^0) - \mathrm{PV\_Y}(D^0))^2 + (\mathrm{END\_VTX\_Y}(D^0) - \mathrm{PV\_Y}(\mathrm{D}^0))^2}. \tag{3.10}$$

  This request is placed in order to exclude D^0 that are produced by the interaction with the VELO itself. The same cut is applied also for the z direction, to remove the interaction region of SMOG. A plot showing the radius on the xy plane can be found in Fig. 3.2;

- the angles between hh ($h = K, \pi$) and the soft pion is used to remove clone tracks. The distributions before the clone track cut are shown in Fig. 3.1.

3.3 Determination of the raw asymmetries

The number of yields is determined through a binned χ^2 fits to the $m(D^0\pi)$ invariant mass spectra, where $m(D^0\pi_s)$ is defined as

$$m(D^0\pi_s) \equiv \sqrt{\left(m_{D^0}^2 + m_\pi^2 + 2\sqrt{m_{D^0}^2 + |\vec{p}_\pi|^2} - 2\vec{p}_{D^0}\cdot\vec{p}_\pi\right)}. \tag{3.11}$$

Variable	**selection requirement**
$m(D^0\pi)$	$[2004.41, 2020.01]$
χ^2_{IP}	< 9
$\text{DLL}_{K\pi}$ of K from D^0	> 5
$\text{DLL}_{K\pi}$ of π from D^0	< -5
$p(D^0)$	$< 190\text{GeV}/c$
$p_{\text{T}}(D^0)$	$< 18\text{GeV}/c$
$\eta(D^0)$	$\in [2, 5]$
$p(\pi_s)$	$< 20\text{GeV}/c$
$p_{\text{T}}(\pi_s)$	$< 2\text{GeV}/c$
$\eta(\pi_s)$	$\in [2, 5]$
R_{xy}	< 3 mm
$\lvert\text{END\_VTX\_Z}(D^0)\rvert$	< 200 mm
$\theta(hh), \theta(\pi_s, h)$	> 0.001
Fiducial requirements	See Eq. 3.8

Table 3.1: Table of all the offline selection cuts

This equation is used because it does not rely on any mass hypothesis on the D^0 decay products. In fact, Eq. 3.11 depends only on the nominal D^0 and π masses [28] and on the reconstructed momenta of the two particles. Given the charge of the soft pion, the sample is divided into $D^{*+}(+)$ and $D^{*-}(-)$. The signal component of the yield is described by the following probability density function

$$\begin{aligned}\mathcal{P}^{\text{sig}}_{\pm} = \Theta(m - m_{\text{trsh}}) \cdot \big[& f_J \mathcal{J}(m; \mu_j, \sigma_J, \delta_J, \gamma_J) + f_1 G(m; \mu_1^{\pm}, \sigma_1) + \\ & + f_2 G(m; \mu_2^{\pm}, \sigma_2) + (1 - f_J - f_1 - f_2) G(m; \mu_3^{\pm}, \sigma_3) \big],\end{aligned} \tag{3.12}$$

where Θ is the Heaviside function which cut any signal that has a mass value lower than the threshold mass $m_{\text{trsh}} = 2004.4\text{MeV}/c^2$. The function $G(m; \mu, \sigma)$ is a Gaussian with mean μ and standard deviation σ while $\mathcal{J}$ is a Johnson function [29] defined as

$$\mathcal{J}(m; \mu_J, \sigma_J, \delta_J, \gamma_J) = \frac{e^{-\frac{1}{2}\left[\gamma_J + \sigma_J \sinh^{-1}\left(\frac{m-\mu_J}{\sigma_J}\right)\right]^2}}{\sqrt{1 + \left(\frac{m-\mu_J}{\sigma_J}\right)^2}}. \tag{3.13}$$

The background PDF is defined as

$$\mathcal{P}^{\text{bkg}}_{\pm} = \Theta(m - m_{\text{trsh}}) \cdot (m - m_{\text{trsh}})^a e^{-b(m - m_{\text{trsh}})}, \tag{3.14}$$

an effective function that shares the same parameters as the signal PDF, where a and b are free parameters in the fit. The same PDFs are used for the D^{*+} and D^{*-} samples, therefore the actual total PDFs for signal and background are

$$\mathcal{P}_{\text{sig}}^{\text{tot}} = \frac{1 + A_{\text{raw}}}{2} \cdot \mathcal{P}_{+}^{\text{sig}} + \frac{1 - A_{\text{raw}}}{2} \cdot \mathcal{P}_{-}^{\text{sig}}, \tag{3.15a}$$

$$\mathcal{P}_{\text{bkg}}^{\text{tot}} = \frac{1 + A_{\text{bkg}}}{2} \cdot \mathcal{P}_{+}^{\text{bkg}} + \frac{1 - A_{\text{bkg}}}{2} \cdot \mathcal{P}_{-}^{\text{sig}}. \tag{3.15b}$$

The total extended PDF is

$$\mathcal{P}(q, m) = \frac{1}{2(N_{\text{sig}}^{\text{tot}} + N_{\text{bkg}}^{\text{tot}})} \left[(1+qA_{\text{raw}})N_{\text{sig}}^{\text{tot}} \cdot \mathcal{P}_{\text{II}}^{\text{sig}}(m) + (1+qA_{\text{bkg}})N_{\text{bkg}}^{\text{tot}} \cdot \mathcal{P}^{\text{bkg}}(m)\right], \tag{3.16}$$

in which q is a discrete quantity that function as a tag, $q = 1 \rightarrow D^{*+}$ and $q = -1 \rightarrow D^{*-}$. The parameters A_{raw} and A_{bkg}, the raw asymmetries of the signal and background components, are defined as

$$A_{\text{raw}} = \frac{N_{\text{sig}}(D^{*+}) - N_{\text{sig}}(D^{*-})}{N_{\text{sig}}^{\text{tot}}}, \tag{3.17a}$$

$$A_{\text{bkg}} = \frac{N_{\text{bkg}}(D^{*+}) - N_{\text{bkg}}(D^{*-})}{N_{\text{bkg}}^{\text{tot}}}, \tag{3.17b}$$

with $N_{\text{sig}}^{\text{tot}}$ and $N_{\text{bkg}}^{\text{tot}}$ representing the total number of yield for signal and background, respectively.

3.4 Measurement of the systematic uncertainty

The source of systematic uncertainty studied in this thesis comes from the signal and background fit model. It is possible that the baseline model described in Sec. 3.3 may bias the final measurement. For this reason an alternative model is defined and a difference with respect to the final results are evaluated. This method could be applied to both signal and background model as it is done in this thesis work. The alternative signal PDF is defined as

$$\begin{aligned}\mathcal{P}_{\pm}^{\text{sig}} = \Theta(m - m_{\text{trsh}}) \cdot \big[&f_1\mathcal{J}_1(m; \mu_1, \sigma_1, \delta_1, \gamma_1) + f_2\mathcal{J}_2(m; \mu_2, \sigma_2, \delta_2, \gamma_2) + \\ &+ f_3\mathcal{J}_3(m; \mu_3, \sigma_3, \delta_3, \gamma_3)\big],\end{aligned} \tag{3.18}$$

where $\mathcal{J}_n$ are Johnson functions, defined in Eq. 3.13. For the background PDF, the following model was used instead

$$\mathcal{P}_{\pm}^{\text{bkg}} = (m - m_{\text{trsh}})^{\frac{1}{2}} + (m - m_{\text{trsh}})^{\frac{3}{2}} + (m - m_{\text{trsh}})^{\frac{5}{2}}. \tag{3.19}$$

The alternative model is used to fit the $D^0 \to K^+K^-$ and $D^0 \to \pi^+\pi^-$ candidates of the nine data blocks (Fig. 3.3-3.4). The statistical error of A_{raw} in each block. is calculated as the sum in quadrature of the individual errors

$$\sigma_{\text{stat},\, i} = \sqrt{\sigma_i^2(K^+K^-) + \sigma_i^2(\pi^+\pi^-)}. \tag{3.20}$$

The total statistical error is

$$\sigma_{\text{stat}} = \frac{1}{\sqrt{\sum_i \sigma^2_{\text{stat, i}}}} \tag{3.21}$$

The output parameters of the fit to data are used to generate $y = 1500$ pseudo experiments, which are fitted with the baseline and the alternative model to evaluate a potential bias on ΔA_{CP} defined as

$$\delta(\Delta A_{CP})_y = \Delta A^{base}_{CP,y} - \Delta A^{alt}_{CP,\, y}. \tag{3.22}$$

A quality check has been implemented to ensure that only acceptable fit results. The conditions for a good fit quaity are:

- `status == 0`, meaning that the minimizer converged.
- `covQual == 3`, which checks for the good quality of the covariant matrix responsible for the evaluation of the errors.
- `edm < 0.001`, which establishes the maximum distance from the minimum in the parameter space.

Initially, the alternative model presented a huge number of parameters left free to float. In addition, the tails of the Johnson functions (δ_J, γ_J) are very small compared to the huge number of background events. This caused instability in the fit results that oscillate inside an interval of good values near the minimum without finding it. To solve the problem, the tail parameters were fixed in the fits. The constant values were taken from the baseline fit analysis. The distribution of the bias from each pseudo experiment follows a Gaussian function (Fig. 3.5), whose standard deviation can be interpreted as the systematic error of the i-th block, $\sigma_{\text{syst},\, i}$. The systematic error for the i-th block is

$$\sigma_{\text{syst},\, i} = \sqrt{\mu_i^2 + \sigma_i^2}. \tag{3.23}$$

The values of systematic uncertainty for each data block are reported in Tab. 3.2. Then, the total error for the given block is obtained as

$$\sigma_i = \sqrt{\sigma^2_{\text{stat},\, i} + \sigma^2_{\text{syst},\, i}}. \tag{3.24}$$

Through error propagation, the total error for all the blocks is

$$\sigma_{\text{tot}} = \frac{1}{\sqrt{\sum_i \sigma_i^2}} \tag{3.25}$$

The systematic error is then determined by subtracting the statistical error from the total one

$$\sigma_{\text{syst}} = \sqrt{\sigma_{\text{tot}}^2 - \sigma_{\text{stat}}^2}. \tag{3.26}$$

The $\delta(\Delta A_{\text{CP}})$ plots for all data blocks are reported in Fig. 3.5, while the values of standard deviations related are written in Tab. 3.2. Following Eq. 3.26, the value of the total systematic uncertainty obtained is:

$$\sigma_{\text{syst}} = 8 \times 10^{-5}, \tag{3.27}$$

which can be compared with the total statistical error $\sigma_{\text{stat}} = 6.4 \times 10^{-4}$.

Block	$\sigma(\mathbf{\Delta A_{CP}^{base}} - \mathbf{\Delta A_{CP}^{alt}})$
1	5×10^{-5}
2	5×10^{-5}
3	8×10^{-5}
4.1	6×10^{-5}
4.2	9×10^{-5}
5	7×10^{-5}
6	7×10^{-5}
7	9×10^{-5}
8	8×10^{-5}

Table 3.2: Systematic error for each data block.

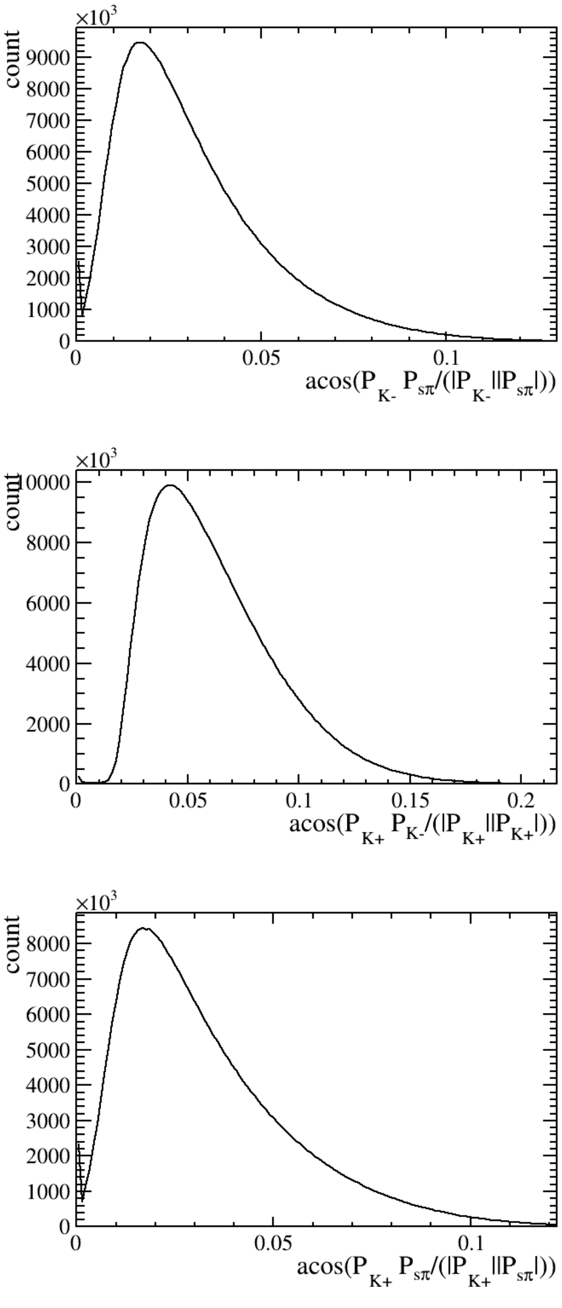

Figure 3.1: Distributions of the angle between $K^-\pi_s$ (top), K^+K^- (middle) and $K^+\pi_s$ (bottom). It is possible to see the background due to clone tracks at angle values close to zero.

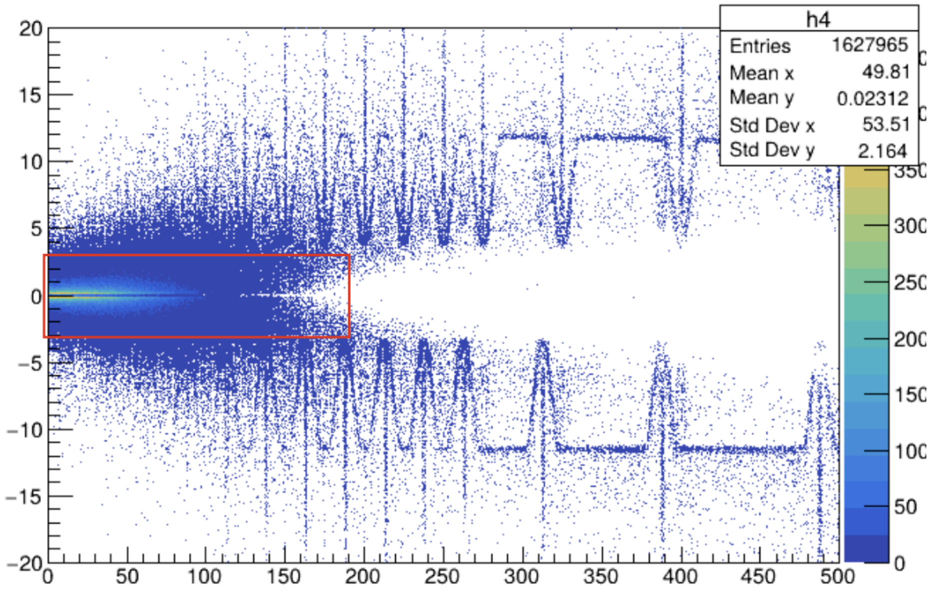

Figure 3.2: xy plane of the VELO detector, with the radius defined in Eq. 3.10 highlighted in red.

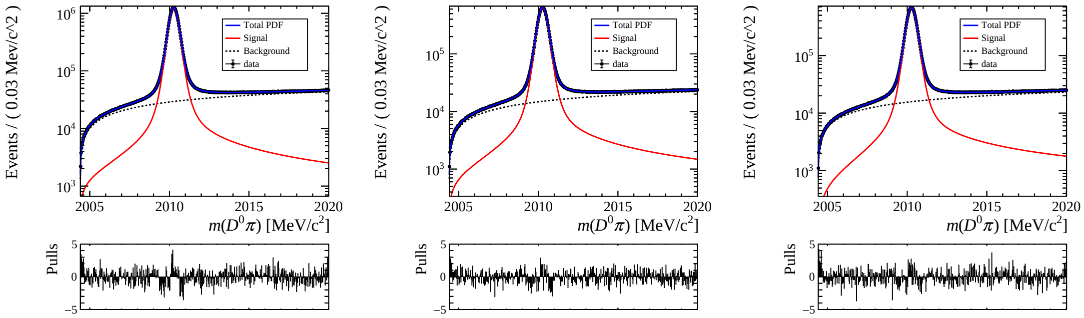

(a) Block 1 KK (b) Block 2 KK (c) Block 3 KK

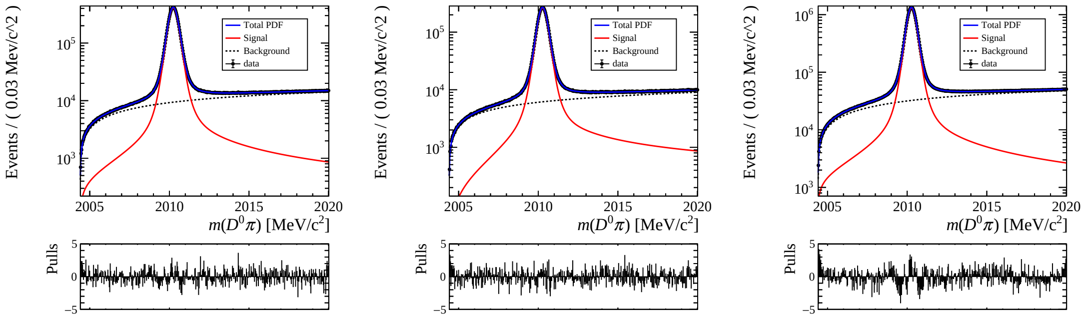

(d) Block 4.1 KK (e) Block 4.2 KK (f) Block 5 KK

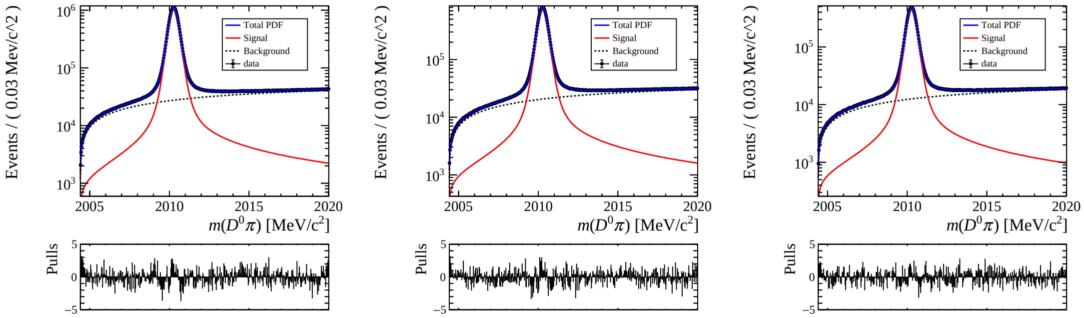

(g) Block 6 KK (h) Block 7 KK (i) Block 8 KK

Figure 3.3: Mass distribution of selected $D^0(K^+K^-)\pi_s$ candidates. The result of the alternative fit to this distribution is also shown.

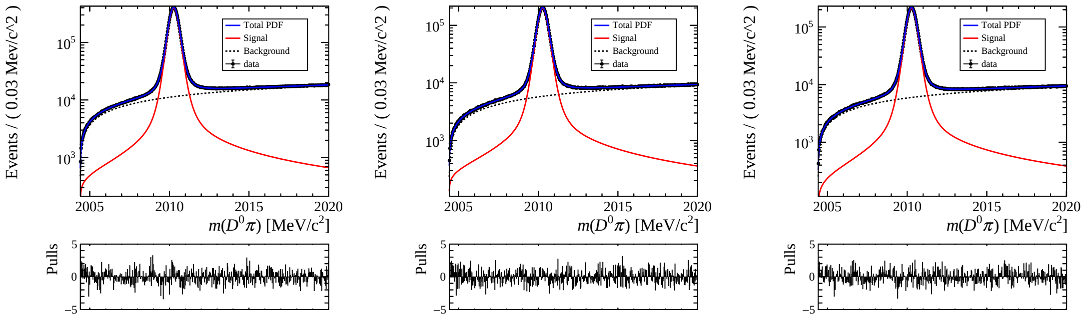

(a) Block 1 pipi (b) Block 2 pipi (c) Block 3 pipi

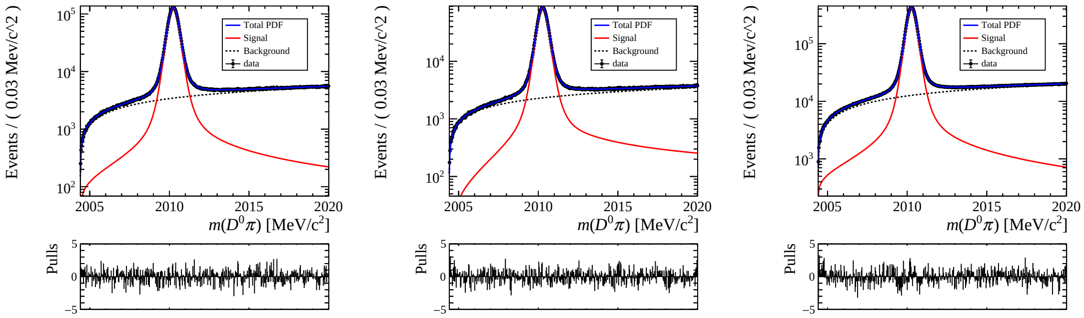

(d) Block 4.1 pipi (e) Block 4.2 pipi (f) Block 5 pipi

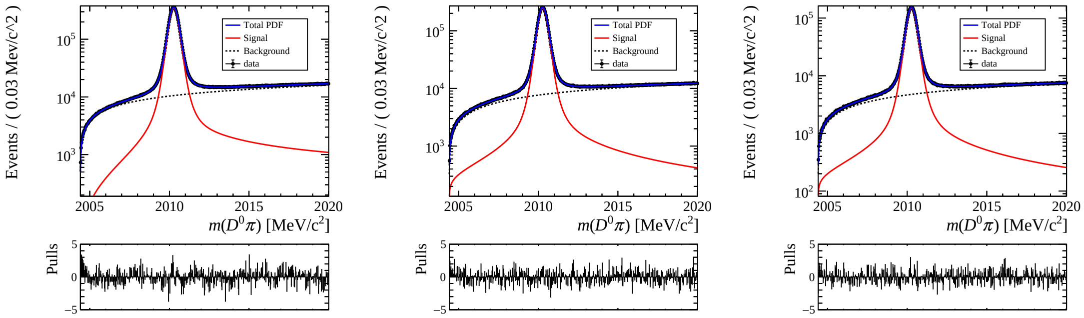

(g) Block 6 pipi (h) Block 7 pipi (i) Block 8 pipi

Figure 3.4: Mass distribution of selected $D^0(\pi^+\pi^-)\pi_s$ candidates. The result of the alternative fit to this distribution is also shown.

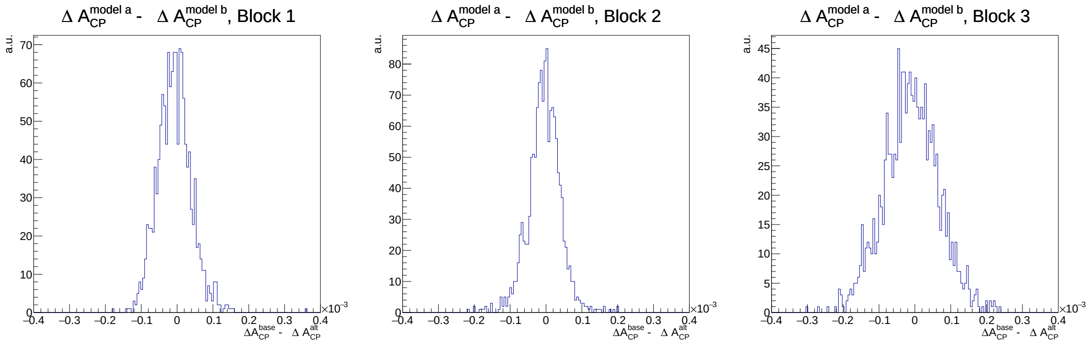

(a) Block 1 (b) Block 2 (c) Block 3

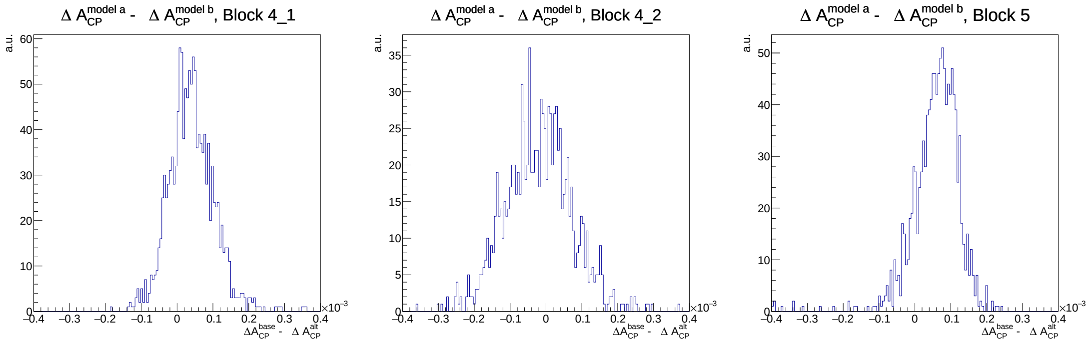

(d) Block 4.1 (e) Block 4.2 (f) Block 5

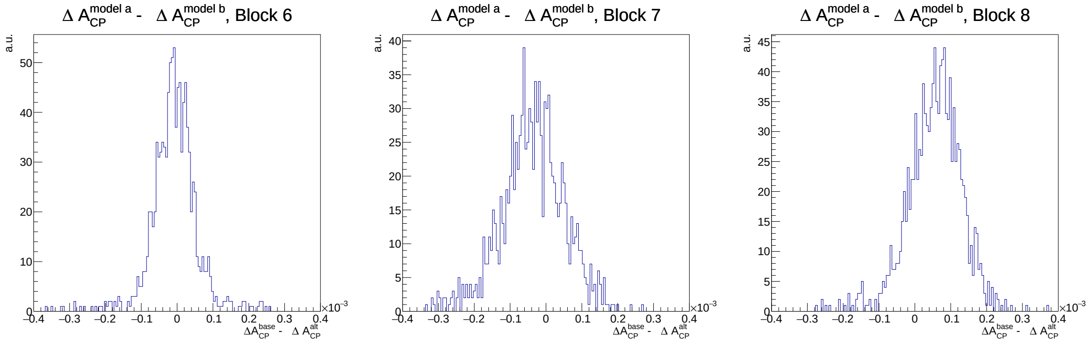

(g) Block 6 (h) Block 7 (i) Block 8

Figure 3.5: Difference between the CP asymmetry computed with the baseline and the alternative model determined from 1500 pseudo experiments.

Conclusions

This thesis presents the measurement of the systematic uncertainty related to the fit model in the ΔA_{CP} measurement using data collected by LHCb during the Run 3 of LHC. An alternative fit model to the $D^0\pi_s$ mass distribution, where D^0 can decay into two pions or kaons, has been developed. A set of 1500 pseudo experiments is generated from the alternative model and fitted with the baseline and the alternative model. For each data block the distribution of the difference between the CP asymmetries of the two models is then used to extract the standard deviation, interpreted as the systematic uncertainty. The uncertainty of each block is used to compute the total systematic uncertainty associated to the baseline model

$$\sigma_{\text{syst}} = 8 \times 10^{-5}, \tag{3.28}$$

which is about one order of magnitude smaller than the total statistical uncertainty.

Bibliography

[1] Abdus Salam. "Weak and Electromagnetic Interactions". In: *Conf. Proc. C* 680519 (1968), pp. 367–377. DOI: `10.1142/9789812795915_0034`.

[2] Steven Weinberg. "A Model of Leptons". In: *Phys. Rev. Lett.* 19 (21 Nov. 1967), pp. 1264–1266. DOI: `10.1103/PhysRevLett.19.1264`. URL: `https://link.aps.org/doi/10.1103/PhysRevLett.19.1264`.

[3] Sheldon L. Glashow. "Partial-symmetries of weak interactions". In: *Nuclear Physics* 22.4 (1961), pp. 579–588. ISSN: 0029-5582. DOI: `https://doi.org/10.1016/0029-5582(61)90469-2`. URL: `https://www.sciencedirect.com/science/article/pii/0029558261904692`.

[4] F. Englert and R. Brout. "Broken Symmetry and the Mass of Gauge Vector Mesons". In: *Phys. Rev. Lett.* 13 (9 Aug. 1964), pp. 321–323. DOI: `10.1103/PhysRevLett.13.321`. URL: `https://link.aps.org/doi/10.1103/PhysRevLett.13.321`.

[5] Peter W. Higgs. "Broken Symmetries and the Masses of Gauge Bosons". In: *Phys. Rev. Lett.* 13 (16 Oct. 1964), pp. 508–509. DOI: `10.1103/PhysRevLett.13.508`. URL: `https://link.aps.org/doi/10.1103/PhysRevLett.13.508`.

[6] D. G. Michael et al. "Observation of Muon Neutrino Disappearance with the MINOS Detectors in the NuMI Neutrino Beam". In: *Phys. Rev. Lett.* 97 (19 Nov. 2006), p. 191801. DOI: `10.1103/PhysRevLett.97.191801`. URL: `https://link.aps.org/doi/10.1103/PhysRevLett.97.191801`.

[7] P. Adamson et al. "Measurement of Neutrino Oscillations with the MINOS Detectors in the NuMI Beam". In: *Phys. Rev. Lett.* 101 (13 Sept. 2008), p. 131802. DOI: `10.1103/PhysRevLett.101.131802`. URL: `https://link.aps.org/doi/10.1103/PhysRevLett.101.131802`.

[8] P. Adamson et al. "Measurement of the Neutrino Mass Splitting and Flavor Mixing by MINOS". In: *Phys. Rev. Lett.* 106 (18 May 2011), p. 181801. DOI: `10.1103/PhysRevLett.106.181801`. URL: `https://link.aps.org/doi/10.1103/PhysRevLett.106.181801`.

[9] K. Abe et al. "First muon-neutrino disappearance study with an off-axis beam". In: *Phys. Rev. D* 85 (3 Feb. 2012), p. 031103. DOI: `10.1103/PhysRevD.85.031103`. URL: `https://link.aps.org/doi/10.1103/PhysRevD.85.031103`.

[10] K. Abe et al. "Measurement of Neutrino Oscillation Parameters from Muon Neutrino Disappearance with an Off-Axis Beam". In: *Phys. Rev. Lett.* 111 (21 Nov. 2013), p. 211803. DOI: `10.1103/PhysRevLett.111.211803`. URL: `https://link.aps.org/doi/10.1103/PhysRevLett.111.211803`.

[11] K. Abe et al. "Evidence for the Appearance of Atmospheric Tau Neutrinos in Super-Kamiokande". In: *Phys. Rev. Lett.* 110 (18 May 2013), p. 181802. DOI: `10.1103/PhysRevLett.110.181802`. URL: `https://link.aps.org/doi/10.1103/PhysRevLett.110.181802`.

[12] N. Agafonova et al. "Final Results of the OPERA Experiment on ν_τ appearance in the CNGS Neutrino Beam". In: *Physical Review Letters* 120.21 (May 2018). ISSN: 1079-7114. DOI: `10.1103/physrevlett.120.211801`. URL: `http://dx.doi.org/10.1103/PhysRevLett.120.211801`.

[13] Nicola Cabibbo. "Unitary Symmetry and Leptonic Decays". In: *Phys. Rev. Lett.* 10 (12 June 1963), pp. 531–533. DOI: `10.1103/PhysRevLett.10.531`. URL: `https://link.aps.org/doi/10.1103/PhysRevLett.10.531`.

[14] Makoto Kobayashi and Toshihide Maskawa. "CP-Violation in the Renormalizable Theory of Weak Interaction". In: *Progress of Theoretical Physics* 49.2 (Feb. 1973), pp. 652–657. ISSN: 0033-068X. DOI: `10.1143/PTP.49.652`. eprint: `https://academic.oup.com/ptp/article-pdf/49/2/652/5257692/49-2-652.pdf`. URL: `https://doi.org/10.1143/PTP.49.652`.

[15] Lincoln Wolfenstein. "Parametrization of the Kobayashi-Maskawa Matrix". In: *Phys. Rev. Lett.* 51 (21 Nov. 1983), pp. 1945–1947. DOI: `10.1103/PhysRevLett.51.1945`. URL: `https://link.aps.org/doi/10.1103/PhysRevLett.51.1945`.

[16] Particle Data Group. "CKM Quark-Mixing Matrix". In: (2024). URL: `https://pdg.lbl.gov/2024/reviews/rpp2024-rev-ckm-matrix.pdf`.

[17] Federico Betti. *Observation of CP violation in charm decays at LHCb*. 2019. arXiv: `1905.05428 [hep-ex]`. URL: `https://arxiv.org/abs/1905.05428`.

[18] *Letter of Intent for the LHCb Upgrade*. Tech. rep. Geneva: CERN, 2011. URL: `https://cds.cern.ch/record/1333091`.

[19] C Fitzpatrick and V V Gligorov. *Anatomy of an upgrade event in the upgrade era, and implications for the LHCb trigger*. Tech. rep. Geneva: CERN, 2014. URL: `https://cds.cern.ch/record/1670985`.

[20] *LHCb Trigger and Online Upgrade Technical Design Report*. Tech. rep. 2014. URL: `https://cds.cern.ch/record/1701361`.

[21] LHCb Collaboration. *LHCb VELO Upgrade Technical Design Report*. Tech. rep. 2013. URL: `https://cds.cern.ch/record/1624070`.

[22] E.A. Papadelis. "Characterisation and Commissioning of the LHCb VELO Detector". PhD thesis. Vrije University, Amsterdam, 2009.

[23] M Alemi et al. "First operation of a hybrid photon detector prototype with electrostatic cross-focussing and integrated silicon pixel readout". In: *Nuclear Instruments and Methods in Physics Research Section A: Accelerators, Spectrometers, Detectors and Associated Equipment* 449.1 (2000), pp. 48–59. ISSN: 0168-9002. DOI: `https://doi.org/10.1016/S0168-9002(99)01448-5`. URL: `https://www.sciencedirect.com/science/article/pii/S0168900299014485`.

[24] R. Aaij et al. "Tesla: An application for real-time data analysis in High Energy Physics". In: *Computer Physics Communications* 208 (2016), pp. 35–42. ISSN: 0010-4655. DOI: `https://doi.org/10.1016/j.cpc.2016.07.022`. URL: `https://www.sciencedirect.com/science/article/pii/S0010465516302107`.

[25] R. Aaij et al. "A comprehensive real-time analysis model at the LHCb experiment". In: *Journal of Instrumentation* 14.04 (Apr. 2019), P04006–P04006. ISSN: 1748-0221. DOI: `10.1088/1748-0221/14/04/p04006`. URL: `http://dx.doi.org/10.1088/1748-0221/14/04/P04006`.

[26] *Computing Model of the Upgrade LHCb experiment*. Tech. rep. Geneva: CERN, 2018. DOI: `10.17181/CERN.Q0P4.570N`. URL: `https://cds.cern.ch/record/2319756`.

[27] R. Aaij et al. "Measurement of the $D^{\pm}$ production asymmetry in 7 TeV pp collisions". In: *Physics Letters B* 718.3 (Jan. 2013), pp. 902–909. ISSN: 0370-2693. DOI: `10.1016/j.physletb.2012.11.038`. URL: `http://dx.doi.org/10.1016/j.physletb.2012.11.038`.

[28] M. Tanabashi et al. "Review of Particle Physics". In: *Phys. Rev. D* 98 (3 Aug. 2018), p. 030001. DOI: `10.1103/PhysRevD.98.030001`. URL: `https://link.aps.org/doi/10.1103/PhysRevD.98.030001`.

[29] N. L. Johnson. “Systems of frequency curves generated by methods of translation”. In: *Biometrika* 36.1-2 (June 1949), pp. 149–176. ISSN: 0006-3444. DOI: `10.1093/biomet/36.1-2.149`. eprint: `https://academic.oup.com/biomet/article-pdf/36/1-2/149/513258/36-1-2-149.pdf`. URL: `https://doi.org/10.1093/biomet/36.1-2.149`.